AB INITIO STUDY OF COHESIVE, ELECTRONIC AND ELASTIC PROPERTIES OF ORDERED CUBIC-BASED Mg-Li ALLOYS

A thesis presented

by

Maje Jacob Phasha

to

The Faculty of Sciences, Health and Agriculture
in fulfillment of the requirements
for the degree of

Master of Science
in the subject of

Physics
University of Limpopo (Turfloop Campus)
(Former University of the North)
Sovenga, South Africa

Supervisor: Professor P.E. Ngoepe
Co-Supervisor: Professor D.G. Pettifor

[May] [2005]

ABSTRACT

Self-consistent electronic structure calculations have been performed on ordered cubic-based magnesium-lithium (Mg_x-Li_{1-x}) alloys spanning the concentration range $0 \leq x \leq 1$, using an ab initio plane wave pseudopotential (PWP) method. The first principle pseudopotential planewave approach is used within the local density approximation (LDA) and generalized-gradient approximation (GGA)of the density functional theory (DFT) framework. We have calculated the binding energy curves and the systematic trends in various cohesive and elastic properties at zero temperature, as a function of Li concentration. The calculated equilibrium lattice parameters show a large deviation from Vegard's rule in the Li-rich region whilst the bulk moduli decrease monotonically with increase in Li concentration. The heats of formation for different ground state superstructures predict that the DO_3, B2 and DO_{22} structures would be the most stable at absolute zero amongst various phases having the Mg_3Li, MgLi and $MgLi_3$ compositions, respectively. This stability is reflected in the electronic density of states (DOS). Because of the special significance of the isotropic bulk modulus, shear modulus, Young's modulus and Poisson's ratio for technological and engineering applications, we have also calculated these quantities from the elastic constants. The elastic constants indicate the softness of the material as more Li is added with

the bcc-based phases becoming mechanically less stable for Li concentration less than 50%. Our results show good agreement within the estimated uncertainty with both experimental and previous theoretical results.

DECLARATION

I declare that the dissertation hereby submitted to the University of Limpopo for the degree of Master of Science has not previously been submitted by me for a degree at this or any other university, that it is my own work both in design and execution, and that all material contained therein has been duly acknowledged.

_____

Maje Jacob Phasha

DEDICATION

This piece of work is dedicated to the following:

My parents, **Maria Ramasela & William Madimetja Phasha**

My aunt, **Esther Masekopo** & uncle, **Andrew Somchesa Mahlangu**

My two beloved brothers, **Malose Thona** & **Frekkie Mashou Phasha**

My grandfather, **Jones Thapedi Matlou**, all my **Ancestors** &

their King Dashe.

Ka Maatla!!!

ACKNOWLEDGEMENTS

I would like to thank various people and organizations who contributed in different ways to make this work a success. I highly appreciate and acknowledge the guidance and courageous support of Prof. P.E. Ngoepe throughout the entire process of this work.

I would like to send my sincere gratitude to Prof. D.G. Pettifor and Dr. D. Nguyen-Mann for their guiding and stimulating discussions as well as valuable and helpful inputs. All members of MMC and Materials Modelling Laboratory (MML), Department of Materials, Oxford University, who contributed in various forms to making this work come through are greatly acknowledged.

The financial support from The National Research Foundation (NRF) of South Africa-Royal Society (RS) of Great Britain collaboration and Council for the Scientific and Industrial Research (CSIR) is greatly acknowledged. The University of the North for providing the state of art Materials Modelling Center (MMC), which is within the School of Physical and Mineral Sciences of Facaulty of Health, Science and Agriculture, with excellent facilities to enable us to perform all our calculations in this work.

Mostly, I am very much thankful to my family and friends who stood by me during difficult and challenging times and also for their patience throughout my period of study.

Lastly, I am greatful to everyone who might have contributed to the success of this work in one way or the other.

Table of Contents

1.1 List of Figures

1.2 List of Tables

Chapter 1
INTRODUCTION

1.1 Background

Over the last two decades, there has been a significant increase in the use of light metals such as Al, Mg, Ti, Li, etc. Furthermore, the consumption rate of these materials is continually increasing due to societal pressures for high performance, lighter structural materials, as well as growing demands for battery materials.

At a density of 1.74 g/cm^3, magnesium is the lightest structural metal, the factor that place it among the front-runners contesting as possible suitable candidates in lightweight industrial applications. In addition to its readily availability, constituting about 2.7% of earth's crust, magnesium offers several advantages including excellent machinability, good castability, good weldability, good creep resistance, high thermal conductivity, and extreme lightness. However, a number of challenging key factors need to be taken into account when considering Mg developments, in particular the hexagonal close-packed (hcp) crystal structure of pure Mg, which seems to limit its use in structural applications, poor corrosion resistance, increasing cost, high electrochemical potential and poor cold workability. Conversely, the situation could be improved by alloy formation with Zn, Li, Al or Mn, leading to a higher specific strength. An addition of a sufficient quantities of lithium, above 10 weight percent, to

magnesium causes an important $hcp \rightarrow bcc$ phase change, which induces the desired improvements in low temperature formability characteristics with less directionality in properties [1]. It also has a positive effect on the density (decreased) and the ductility and damage tolerance (both increased) of the material. These properties render magnesium-lithium alloys as a very suitable class of candidates for substitution of other lightweight structural materials (like aluminum or fibre-reinforced plastics) in diverse industrial applications: commercial products such as computer housing, parts for the automotive and aerospace industry, where reduction in the intrinsic weight of the design is of vital importance [2]. Due to the favourable properties, magnesium technology is part of a general attempt to obtain a new generation of lighter, more fuel efficient and less polluting (less CO_2 emmission) vehicles. This goal implies a multidisciplinary approach in which engineering, physics and chemistry, each must converge in defining the characteristics of the components made out of light materials.

The high stiffness strength of Mg is owed to the element's hcp structure which also makes it difficult to apply slipping modes in the useful engineering directions. The alloying element, which causes a useful phase change to bcc is lithium [3], as shown by the phase diagram in Figure 1.1 [4]. Lithium, the lightest metal with a simple elemental electronic configuration and a broad range of practical applications, has naturally been the subject of both theoretical and experimental investigations for a long time. Yet its electronic and structural properties remain enigmatic to this

day [5]. Like other alkali metals it has a bcc room temperature structure, but upon cooling at low temperatures it undergoes a martensitic transformation around 80 K. The transformation was first observed very early [6, 7], but the crystal structure of the low-temperature phases of Li have led to some controversy and remained a subject of debate for several decades. Later, on the basis of additional data [8], Overhauser [9] proposed that the neutron scattering data were consistent with the 9R structure, a close-packed phase with nine-layer stacking sequence. Subsequent investigations in several sets of neutron scattering data confirmed 9R as the primary structure at low temperature [10]. More recently, analysis of diffuse neutron scattering data [11] has led to the opinion that below 80 K a disordered polytype structure, consisting of the short-range correlated fcc and hcp phases, coexists with the longer-ranged, ordered 9R structure. Furthermore, upon heating, the 9R phase and the disordered polytype appear to transform first to an ordered fcc phase before reverting to bcc Li above 150 K [11].

It was not until the early 1930s that the development of magnesium-lithium alloys started, as illustrated in Figure 1.2 [12]. Ultralight magnesium-lithium alloys provide a promising basis for the development of structural metallic materials with a high strength-to-weight ratio [13]. The effect of Li addition has gained considerable importance because it not only makes the Mg-Li alloy lighter (density reduction from 1.74 g/cm^3 to about 1.30 g/cm^3), but also increases the values of the elastic constants, which cannot be improved using conventional alloying techniques. Exper-

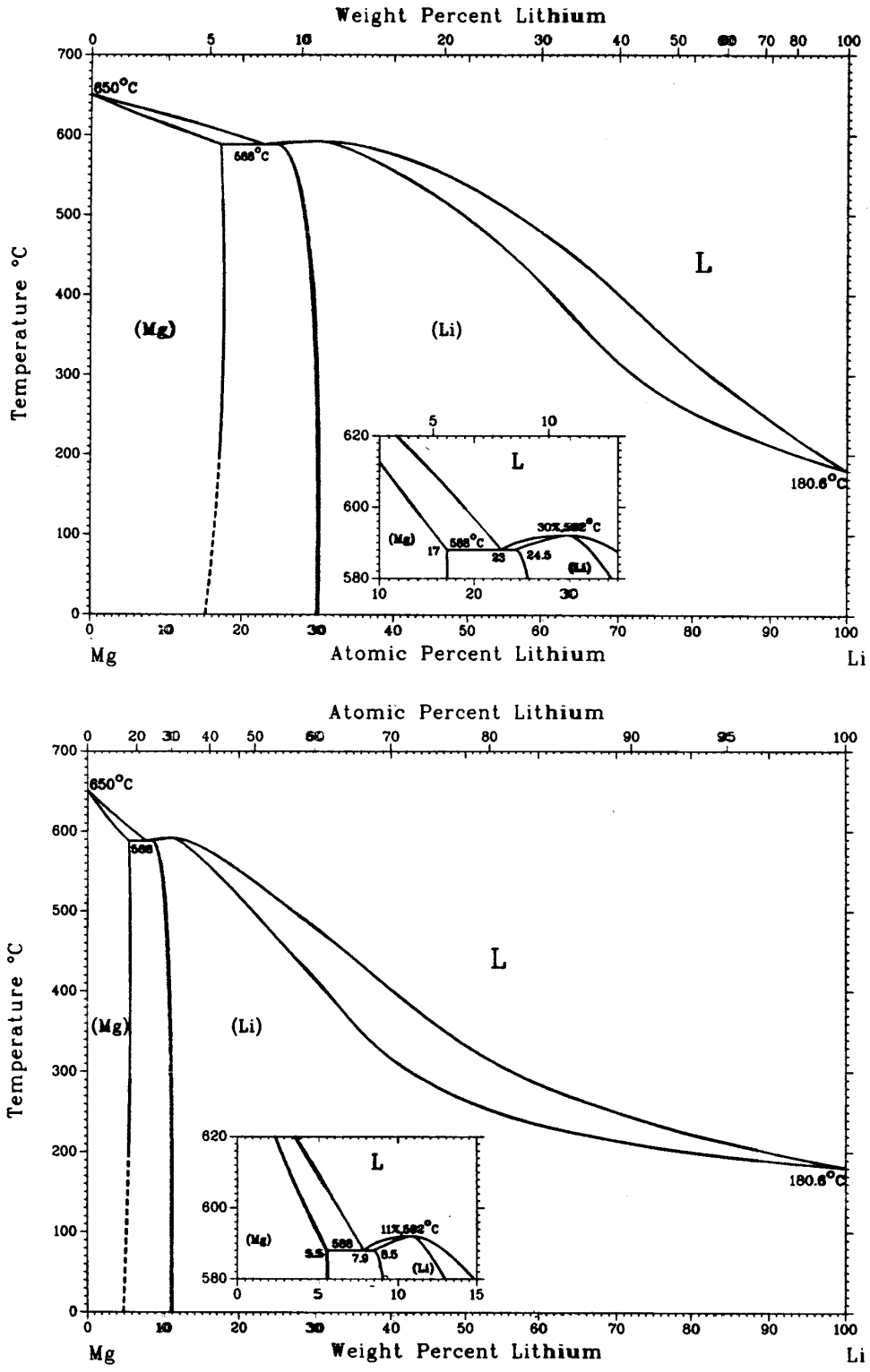

Figure 1.1: Mg-Li phase diagram [4].

imentally, the solubility of other alloying elements in magnesium is limited, restricting the possibility of improving the mechanical properties and chemical behaviour [3]. However, numerous difficulties were encountered which were associated with melting and casting, instability of mechanical properties at room temperature, poor corrosion resistance and excessive creep at relatively low stresses [14]. The development of these alloys was subsequently abandoned during the mid 1940s because it was only possible to produce Mg-Li alloys which were unstable or stable but not strong [15]. The strengthening mechanism of this alloy system was not completely understood, which led to the failure of developing these alloys into a potential material for aerospace industries [14].

Recently experimental and theoretical studies of light metal alloys are increasing owing to their usage in the automotive and aerospace industries [13]. The technological challenge is to produce high-stiffness materials with suitable mechanical properties. First-principles electronic structure calculations can predict accurate elastic moduli, from which we may infer the degree of ductility of different cubic alloys [16]. In cubic crystals the ratio C'/B of shear to bulk modulus has provided a useful criterion for ductility or brittlement. FCC and BCC metal crystals are generally intrinsically ductile when $C'/B < 0.4$ and brittle when $C'/B > 0.5$ [16, 17]. In addition, they lead to a proper understanding of the structural competition between the various stable and metastable alloy phases. The predicted heats of formation with respect to different underlying lattices such as fcc or bcc are essential input for calcu-

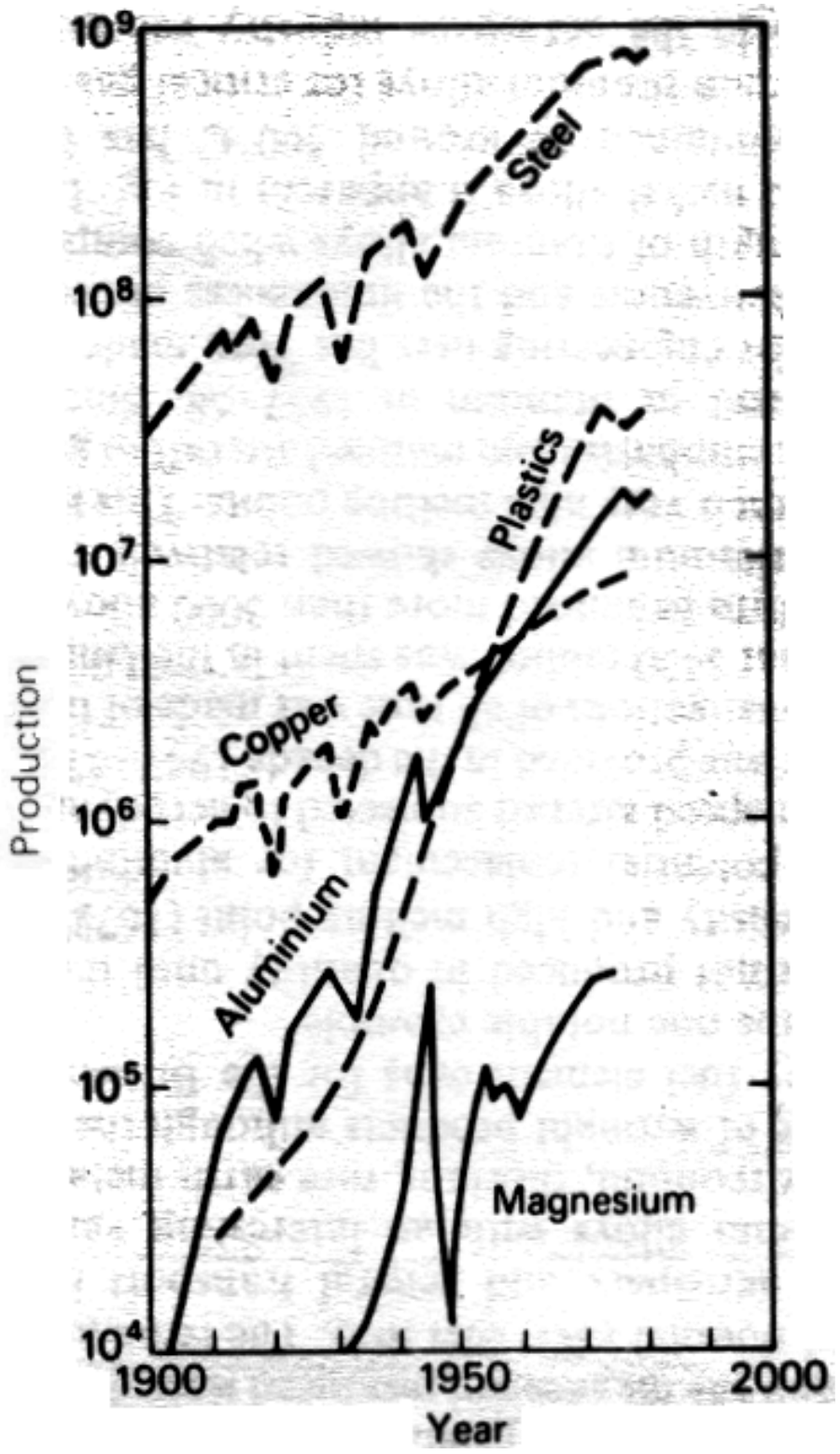

Figure 1.2: World production trends for various metals and plastics [12].

lating effective cluster interactions [18], from which theoretical phase diagrams can be computed using Monte Carlo [19] or the Cluster Variation Method (CVM) [20]. At the centre of this computational approach lies the attempt to simulate and predict the properties of ordered cubic-based magnesium-lithium (Mg_xLi_{1-x}) binary alloys spanning the concentration range $0 \leq x \leq 1$.

There is a growing interest in combining quantum mechanical electron theory with statistical mechanics, in order to arrive at a first principle description of configurational thermodynamics in metallic alloys [21]. The idea is to get the configurational entropy corresponding to a certain alloy composition by starting from an Ising Hamiltonian [22] in which the many-body cluster interactions are obtained from electron theory. In this method, one first obtains the relative stabilities of the ordered equilibrium (stable) phases as well as of the various possible phases which are difficult to probe experimentally. The essential prerequisite is to have a reliable and efficient electronic structure method for calculation of the heat of formation of a large number of ordered superstructures of binary alloys. In addition to this progress in materials modelling at the electronic level, there have been significant developments in computational micromechanics and damage mechanics techniques at the continuum level. These simulations are usually finite element based and compute the mechanical properties of alloys such as the stress distributions around cracks.

Moreover, Mg-Li alloys are also seen as viable candidates for an efficient alloy battery system [23]. While the high activity of lithium makes it attractive as a

unique energy source for microelectronic devices, a critical issue plaguing existing lithium batteries is the cycleability of the lithium electrodes, and hence, the rechargebility of the battery system. The formation of a dendritic structure during charging is one of the major problems associated with pure lithium used as the negative electrode in a secondary lithium battery. Typically, dendrite growth worsens progressively during cycling, often leading to both disconnection and electrical isolation of the active lithium or electrical shorting between electrodes. Lithium intercalation materials, such as lithiated carbon, LiAl alloys, and Sn-based composite oxides, have been studied to replace pure lithium in an effort to reduce the tendency for lithium dendrite formation. The diffusion coefficients for lithium in the Mg-Li alloy electrodes were found to be of two to three orders of magnitude larger than those in other lithium alloy systems (*e.g.* LiAl). Mg-Li alloy electrodes also appear to show not only the potential for higher rate capabilities (power densities) but also for larger capacities (energy densities) which might considerably exceed those of lithiated carbon or Sn-based electrodes for lithium batteries [23].

1.2 Rationale and Objectives

Owing to their low density, magnesium alloys are the lightest metallic materials for construction ever known. They are thus extremely attractive for researchers concerning lightweight applications, possibly substituting in the future aluminium alloys as well as fibre-reinforced plastics. The main aim is to expand the application of mag-

nesium by alloying it with lithium. This group of alloys, to which little attention has been paid in the past, provides an increased ductility at a comparatively high thermochemical stability. Metallurgical and processing measures have preferably aimed at a mechanical strengthening of the MgLi-matrix. At the same time the ductility properties were to be retained to a large extent to preserve a balanced mechanical behaviour [24]. In addition, magnesium is the eighth mostly abundant metal in nature, constituting about 2.7% of earth crust [12], though it is becoming more costly on the other hand due to its technological promises.

The objectives of this thesis are:

(i) to investigate the electronic and structural properties of a series of ordered superstructures of binary magnesium-lithium ($Mg_{1-x}Li_x$) alloys with respect to the underlying fcc and bcc lattice, using *ab initio* [25, 26] electronic structure techniques, in particular the plave-wave pseudopotential (PWP) method embodied in the CASTEP code.

(ii) to evaluate the elastic moduli of these alloys.

1.3 Outline of the dissertation

In this chapter the material under consideration and the content of this dissertation have been introduced and our aims and objectives clearly stated. In the next chapter , we review various computational modelling techniques, in particular density functional theory (DFT) approaches. In Chapter 3 the plane-wave code, which is used to

solve the electronic structure, is outlined . The theory of practically simulated results as well as the structural and electronic results of the current study are presented and discussed in Chapter 4 and 5, respectively. Finally, in Chapter 6 we summarize our work by making some conclusions and recomendations for future work.

Chapter 2
THEORETICAL TECHNIQUES

2.1 Introduction

Computer simulation techniques offer an alternative way of investigating properties of materials (using computers), whereby the simulator builds a model of a real system and explores its behaviour. The mathematical model is physically based with the exploration being done on a computer. In many ways these simulation studies share the same mentality as experimental investigations. However, in a simulation there is absolute control and access to detail, and given enough computer muscle, exact answers for the model.

The fundamental atomistic principles underlying the structural and functional behaviour of materials are astonishingly simple: (a) For most purposes, atomic nuclei can be treated as classical particles with a given mass and positive charge, (b) electrons are particles of spin one half, thus obeying the Pauli exclusion principle, their kinetic behaviour is described by quantum mechanics, and (c) the only relevant interactions are of an electrodynamic nature, in particular, attractions and repulsions governed by Coulomb's law. Based on these fundamental principles it is conceptually possible to explain and predict the wonderful richness of most physical and all chemical properties of matter such as the structure and stability of crystalline phases,

the mechanical properties of alloys, the magnetic properties of transition metals and so on. This development in first principle theory has opened up many exciting possibilities for the study of condensed matter since one is now in a position to predict properties of systems which were formerly inaccessible to theory and sometimes experiment.

Several factors have contributed to the present success of ab initio calculations for real materials systems. The first is the formalism of density functional theory (DFT) [27] and continuing development of approximations to the DFT formalism for electron exchange and correlation. The second is the subsequent advent of modern high speed computers (enormous increase in computational power). This has made it possible to carry out calculations on real materials in interesting situations with sufficient accuracy that there can be meaningful detailed comparison with experimental measurements. The third is the refinement in band structure calculation techniques and the invention of the *ab initio* pseudopotentials [25], which have led to rapid computation of total energies. The density functional method has made it feasible to calculate the ground state energy and charge density with remarkably accurate results for real solids. This is the starting point for almost all current first-principle calculations of total energies of solids. Finally, there have been significant new development in experimental techniques and materials preparation that are making it possible to probe the structure of matter in ways never realized before. One advance is the ability to create high pressures and explore the properties of matter over a wide

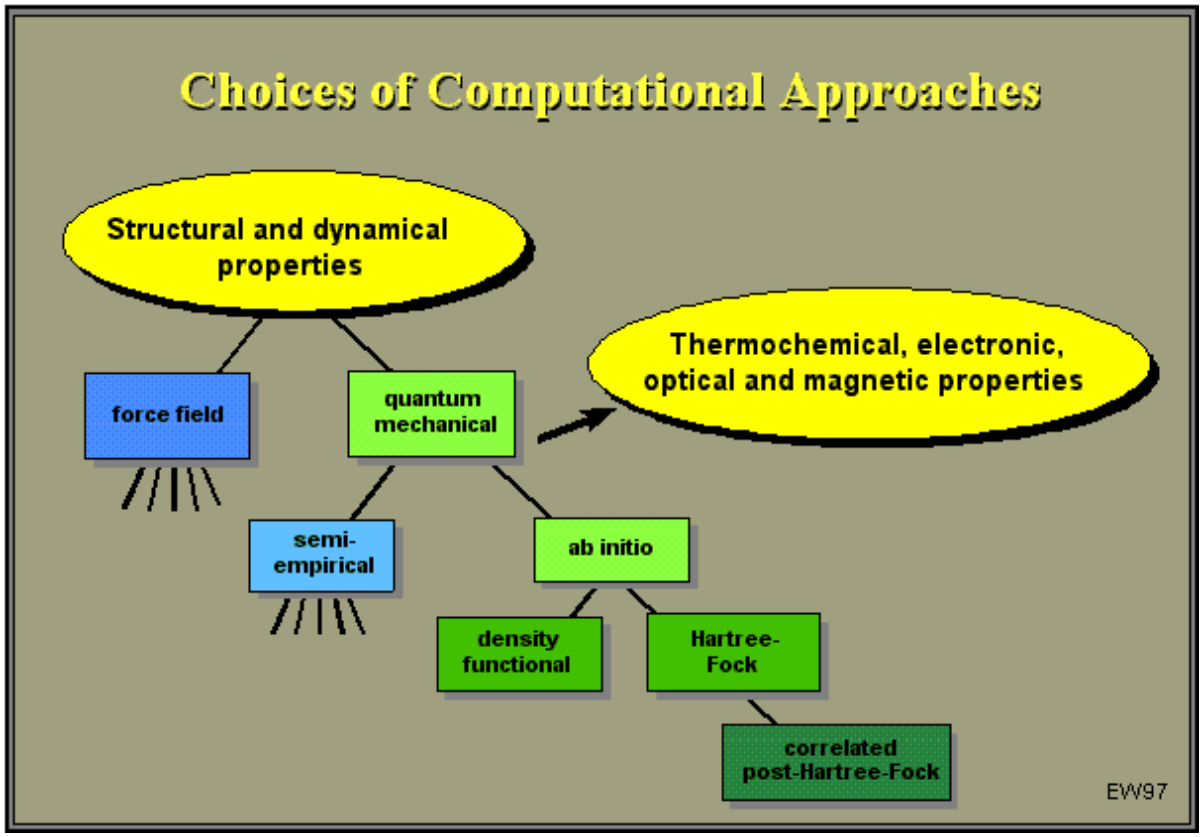

Figure 2.1: Major atomistic approaches for the simulation and prediction of structural and functional properties [29]

range of densities [28]. This is an ideal experimental tool to provide information that can be compared directly with current theoretical calculations.

Atomistic simulation has become a valued technique in predicting the properties of materials. Computer modelling at this level is based on two types of approach, namely: the force field or empirical potential methods and quantum mechanical methods. The major atomistic approaches for the simulation and prediction of structural and functional properties are shown in Figure 2.1 [29]. The first decision

is between quantum mechanical and force field methods. Although, force field methods are preferable because of the high computational efficiency, they have not been successfully developed for metallic alloys and the prediction of their phase diagrams, so that we must use a quantum mechanical based approach for our research on Mg-Li alloys. Such an approach can be treated semi-empirically within a tight-binding model [30] or within a nearly-free-electron model using second-order perturbation theory [31]. In this thesis, however, we rely on more accurate *ab initio* methods, in particular density functional theory.

2.1.1 Evolution of DFT methods

This historical review relies heavily on the excellent article by Wimmer [29]. Prior to the developments of density functional theory, the calculation of energy band structures for crystalline solids had become a major goal of computational solid state physics. As shown in Figure 2.2 [29], during the 1960's, when quantum chemists began systematic Hartree-Fock studies on small molecules, energy band structure calculations of solids were possible only for simple systems such as crystals of copper and silicon containing one or a few atoms per unit cell. The aim of these efforts in solid state physics were different from those of quantum chemistry. Whereas quantum chemistry focused on the *ab initio* determination of molecular structures and energies, the goal of energy band structure calculations for solids was the understanding of conducting and insulating behaviour, the elucidation of the types of bonding, the

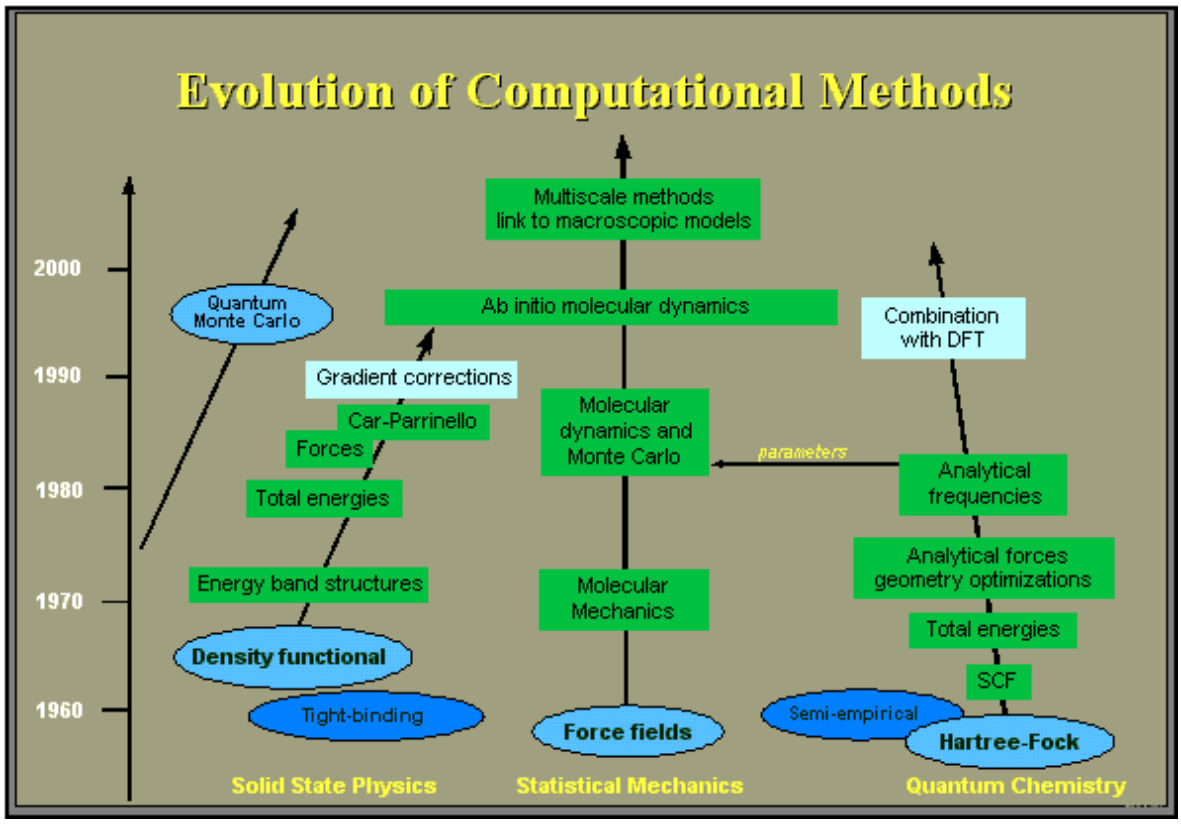

Figure 2.2: Evolution of DFT methods [29]

prediction of electronic excitations such as energy band gaps, and the interpretation of photoexcitation spectra [29].

To this end, semiempirical pseudopotential theory [32, 33] became a successful and pragmatic approach especially for semiconductors. All-electron band structure calculations were applied mostly to transition metals and their compounds. Initially, these calculations were carried out non-self-consistently. For a given crystal structure and atomic positions in the lattice, a crystal potential was constructed from superposed atomic densities and the energy bands evaluated for selected points in momen-

tum space without improving the electron density through a self-consistency procedure. The shape of the crystal potential was simplified in the form of a "muffin-tin" potential [34] with a spherical symmetric potential around the atoms and a constant potential between the atomic spheres. For close-packed structures such as fcc Cu, this is an excellent approximation and substantially simplifies the calculation of the energy bands. During the 1960's, self-consistency was introduced still using the simplified "muffin-tin" potential. Around 1970, self-consistent muffin-tin energy band structure calculations were possible for systems containing a few atoms per unit cell. At that time, quantum chemists had already recognized the power of total energies as a tool for geometry optimization of molecules and had developed analytic energy gradients (forces) that greatly facilitated geometry optimizations. Shape approximations to the potential are questionable for open molecular structures and hence the use of the muffin-tin approximation in the form of the so-called multiple-scattering X-alpha method [35] for molecules and clusters met with skepticism among many ab initio quantum chemists.

In computational solid state physics, total energy calculations as a predictive tool for crystal structures and elastic properties of solids came into general use only in the mid to late 1970's, which was almost 10 years later than the corresponding application of the Hartree-Fock method to molecules.

By 1970, density functional theory had become a widely accepted many-body approach for first-principles calculations on solids, superceding the X-alpha-approach.

Initially, energy band structure methods such as the augmented plane wave (APW) method [34] and the Korringa-Kohn-Rostoker (KKR) method, [36, 37] were very tedious since the system of equations to be solved in each iterative step of the self-consistency procedure were nonlinear (the matrix elements depended on the energy). Furthermore, the computer hardware at that time was limited both in processor speed, but perhaps even more by memory size. A major step forward was the introduction of linearized methods, especially the linearized augmented plane wave (LAPW) method [38, 39], and the linearized muffin-tin orbital (LMTO) method [39].

By 1980, quantum chemists had developed analytical second derivatives in Hartree-Fock theory for the investigation of structural and vibrational properties of molecules. During the same time, computational solid state physicists worked on the formulation of all-electron self-consistent methods without muffin-tin shape approximations, such as the full-potential linearized augmented plane wave (FLAPW) method with total energy capabilities as reviewed by Wimmer et al. [40]. Analytic first derivatives (forces) within solid state calculations were first introduced in pseudopotential plane wave methods as reviewed by Payne et al [25] and only fairly recently in other solid state methods. Larger unit cells of bulk solids with more degrees of freedom and especially the investigation of surfaces required tools for predicting the position of atoms, for example in the case of surface reconstructions. Hence, total energy and force methods for solids and surfaces became more urgent.

In solid state calculations, the emphasis had shifted from the prediction of electronic structure effects for a given atomic arrangement to the prediction of structural and energetic properties as revealed by novel techniques such as extended x-ray absorption fine structure spectroscopy (EXAFS) and the scanning tunneling microscope (STM). Pseudopotential theory, originally used in the form of a parameterized semi-empirical approach for calculating energy band structures of semiconductors, had been developed into a first-principles method with rigorous procedures to construct reliable pseudopotentials [41]. Pseudopotentials turned out to be particularly elegant and useful for the investigation of main-group element semiconductors. Using the pseudopotential plane wave approach, Car and Parrinello [42] made an important step in the unification of electronic structure theory and statistical mechanics. In this approach, it is possible to simulate the motions of the atomic nuclei as they would occur, for example, in a chemical reaction while at the same time relaxing the electronic structure, all within a single theoretical framework. Until then, molecular dynamics had been mostly the domain of empirical force field approaches which are not intended for describing the formation and breaking of chemical bonds.

Density functional theory, originally intended for metallic solid state systems, turned out to be also surprisingly successful for describing the structure and energetics of molecules. First clear evidence for the capabilities of the local density functional approach for molecular systems was given already in the 1970's, but only recent systematic calculations on a large number of typical molecules together with

the introduction of gradient corrected density functionals [43] have made density functional theory an accepted approach for quantum chemistry [44]. These capabilities of density functional theory as a tool for molecular and chemical problems is remarkable, since the theory was originally developed as an approximate approach in solid state physics. In this work we have based our approach the density functional theory.

2.1.2 Semiempirical methods

These are approximate methods which make use of a simplified form of Hamiltonian as well as adjustable parameters with values obtained from fitting to both experimental and first principles data. Even with increases in computer speed and memory and the development of efficient algorithms, *ab initio* methods are not applied routinely to unit cells with more than dozen atoms. On the other hand, semiempirical methods are fast enough to be applied routinely to larger systems. Thus, semiempirical methods make electronic structure calculations available for a wider range of systems.

In materials science a widely-used semi-empirical approach is the tight-binding model [30] in which the bond or hopping integrals are parameterized following the seminal paper by Slater and Koster [45]. This method has been successfully developed into a powerful tool for the study of semiconductors and transition metals, in particular, the interplay between their structural and electronic properties with de-

fects, surfaces, and interfaces (see, for example [46]). Currently significant efforts are being made to improve the speed of tight-binding methods in order to study dynamic processes such as the deposition of Ag atoms on Cu surfaces [47] and the effect of irradiation on the stability of materials [48].

The real-space tight-binding recursion method, which was developed in the early 1970's [49, 50], presents a promising framework for the fast evaluation of total energies and forces, since its computational time scales as order N rather than N^3 as for **k**-space approaches (where N is the number of atoms in the unit cell, and **k** is a point within the first Brillouin zone of the periodic cell). A novel scheme by Aoki [51], which generalizes the bond order formalism by Pettifor [52], leads to a rapidly convergent bond order expansion for transition metals, thus overcoming some of the earlier difficulties of this approach. This approach has been applied to the investigation of dislocation cores [53] and Peierls barriers in technologically important high-temperature intermetallics [54].

2.2 The Hartree-Fock Method

The Hartree-Fock [55, 56] method focuses on the many-body wave functions $\Psi(\overline{r}_1, \overline{r}_2, ..., \overline{r}_N)$ (where the $\overline{r}_1$ denotes the coordinates of the 1st electron, $\overline{r}_2$ the 2nd electron, and so on) that enter the time-independent Schrödinger equation for the system:

$$\hat{H}\Psi_k(\overline{r}_1, \overline{r}_2, ..., \overline{r}_N) = E_k\Psi_k(\overline{r}_1, \overline{r}_2, ..., \overline{r}_N) \tag{2.1}$$

where $\hat{H}$ is the Hamiltonian, i.e., the operator with corresponding eigenvalues E_k and eigenfunctions Ψ_k, whereas $\mathbf{k}$ is a point in space. The Hamiltonian operator consists of a sum of three terms:

$$\hat{H} = \hat{T}_e + \hat{U}_{ext} + \hat{U}_{ee} \tag{2.2}$$

where the kinetic energy of the electrons, the interaction with an external potential and the Coulombic electron-electron interaction, can be written respectively as:

$$\hat{T}_e = -\frac{1}{2}\sum_i \nabla_i^2 \tag{2.3}$$

$$\hat{U}_{ext} = -\sum_{\alpha}^{N_{at}} \frac{Z_\alpha}{|\overline{r}_i - \overline{R}_\alpha|} \tag{2.4}$$

$$\hat{U}_{ee} = \frac{1}{2}\sum_{i\neq j} \frac{1}{|\overline{r}_i - \overline{r}_j|} \tag{2.5}$$

In most simulations of materials the external potential of interest is simply the interaction of the electrons with the atomic nuclei of charge Z_α and position $\overline{R_\alpha}$. In this chapter we use atomic units, so that $e^2 = \hbar = m = 1$ where e is the electronic charge, $\hbar$ is Planck's constant, and m is the electronic mass. The unit of energy is, therefore, the Hartree (where 1 Hartree = 2 Rydbergs = 27.2116 eV) and the unit of length is the first Bohr radius (so that 1 au = 0.529 Å).

When the Schrödinger equation is solved exactly (e.g., for the hydrogen atom), the resulting eigenfunctions Ψ_k form a complete set of functions. The eigenfunction Ψ_0 corresponding to the lowest energy E_0, describes the ground state of the system,

and higher energy values correspond to excited states. Once the function Ψ is known, the corresponding energy of the system can be calculated as an expectation value of the Hamiltonian $\hat{H}$, as:

$$E[\Psi] = \int \Psi^* \hat{H} \Psi dr = \langle \Psi \,|H|\, \Psi \rangle \tag{2.6}$$

where the integration is over (two electron) coordinate space and the notation $[\Psi]$ emphasizes the fact that the energy is a *functional* of the wave function. The energy is always higher than that of the ground state unless Ψ corresponds to Ψ_0, since by the variational theorem:

$$E[\Psi] \geq E_0 \tag{2.7}$$

Once the function Ψ for a given state of the system is known, then the expectation value of any quantity for which the operator can be written down, can be calculated.

In general, the Schrödinger equation cannot be solved exactly. Therefore, approximations have to be used. The first successful attempt to derive approximate wave functions for atoms was devised by Hartree in 1928. He approximated the many-electron wave function Ψ by the product of one-electron functions ϕ for each of the N electrons:

$$\Psi(\overline{r}_1, \overline{r}_2, ..., \overline{r}_N) = \phi_1(\overline{r}_1)\phi_2(\overline{r}_2)...\phi_N(\overline{r}_N) \tag{2.8}$$

In this equation, $\overline{r}_i$ are assumed to contain both the positional coordinates and the spin coordinate of electron i.

The Hartree approximation treats the electrons as distinguishable particles. In 1930 Fock correctly treated the electrons as indistinguishable by proposing an anti-symmetrized many-electron wave function in the form of a Slater determinant [61]:

$$\Psi_{HF} = \frac{1}{\sqrt{N!}} \begin{vmatrix} \phi_1(\overline{r}_1) & \phi_2(\overline{r}_1) & ... & \phi_N(\overline{r}_1) \\ \phi_1(\overline{r}_2) & \phi_2(\overline{r}_2) & ... & \phi_N(\overline{r}_2) \\ . & . & . & . \\ . & . & . & . \\ . & . & . & . \\ \phi_1(\overline{r}_N) & \phi_2(\overline{r}_N) & ... & \phi_N(\overline{r}_N) \end{vmatrix} \tag{2.9}$$

where det indicates a matrix determinant. This single determinant wavefunction accounts for some basic fermion characteristics such as Pauli's exclusion principle, which introduces the new term of *electron exchange*. Within this so-called Hartree-Fock method, the expectation value of the total energy is given by:

$$E_{HF} = \langle \Psi | H | \Psi \rangle = \sum_{i=1}^{N} H_i + \frac{1}{2} \sum_{i=1}^{N} \sum_{j=1}^{N} (J_{ij} - K_{ij}) \tag{2.10}$$

where

$$H_i = \int \phi_i^*(\overline{r})[-\frac{1}{2}\nabla_i^2 + \hat{U}_i]\phi_i(\overline{r})d\overline{r} \tag{2.11}$$

is an element of the one-electron operator $\hat{h}_i$ defined by:

$$\hat{h}_i = -\frac{1}{2}\nabla_i^2 - \sum_{\alpha=1}^{N_{nucl}} \frac{Z_\alpha}{|\overline{r}_i - \overline{R}_\alpha|} \tag{2.12}$$

where N_{nucl} is the total number of nuclei in the material. The J_{ij}'s represent the Coulomb interaction between electron i and electron j. They are called Coulomb integrals and are given by:

$$J_{ij} = \int\int \frac{\rho_i(\overline{r}_1)\rho_j(\overline{r}_2)}{|\overline{r}_1 - \overline{r}_2|} d\overline{r}_1 d\overline{r}_2 = \int\int \phi_i^*(\overline{r}_1)\phi_j^*(\overline{r}_2)\frac{1}{|\overline{r}_1 - \overline{r}_2|}\phi_i(\overline{r}_1)\phi_j(\overline{r}_2) d\overline{r}_1 d\overline{r}_2 \tag{2.13}$$

The inclusion of Pauli's exclusion principle within the Slater determinant leads to an additional term K_{ij}, the so-called exchange integral, which is defined by

$$Kij = \int\int \phi_i^*(\overline{r}_1)\phi_j(\overline{r}_1)\frac{1}{|\overline{r}_1 - \overline{r}_2|}\phi_i(\overline{r}_2)\phi_j^*(\overline{r}_2) d\overline{r}_1 d\overline{r}_2 \tag{2.14}$$

We see that K_{ij} is similar in form to the J_{ij} but the functions ϕ_i and ϕ_j have been exchanged. It follows that electrons i and j have to be of the same spin for K_{ij} to be nonzero due to the orthogonality of their spin parts.

The Hartree-Fock (HF) approximation has been favoured among chemists for calculating the electronic structure of small molecules with a high accuracy. Importantly, the HF results can systematically be improved by applying the configuration interaction (HF-CI) techniques or Møller-Plesset perturbation theory (MP2 or MP4) [57, 58]. Unfortunately, the HF method resulted in a vanishing density of states at the Fermi level in the bulk free electron gas, so that this approximation was avoided by solid state physicists. In turn, they turned to methods based on the electronic density of the material that Thomas and Fermi had proposed at about the same time as

Hartree. They had derived a differential equation for the density without resorting to one-electron orbitals [59, 60]. The Thomas-Fermi (TF) approximation was actually too crude because it did not include exchange and correlation effects and was also unable to sustain bound states because of the approximation used for the kinetic energy of the electrons. However it set up the basis for the later developments of density functional theory (DFT), which has been the way of choice in electronic structure calculations in condensed matter physics during the past three decades and recently, it also became accepted by the quantum chemistry community because of its computational advantages compared to HF-based methods [61, 62].

2.3 Density Functional Theory

Density Functional Theory (DFT) focuses on the electronic density of the system $\rho(\overline{r})$. In their seminal paper of 1964 Hohenberg and Kohn [27] proved two key theorems:

Theorem 1 The total ground state energy E of an electron system is a unique functional of the electron density, i.e.

$$E = E[\rho] \tag{2.15}$$

Theorem 2 This energy functional takes its minimun value E_0 for the correct ground state density $\rho_0(\overline{r})$ under variations in the electron density $\rho(\overline{r})$ such that the

number of electrons is kept fixed, i.e.

$$E_0 \leq E[\rho] \tag{2.16}$$

for which

$$\int \rho(\overline{r})d\overline{r} = N \tag{2.17}$$

where N is the number of electrons in the system. The equality in Eq. (2.16) occurs if and only if $\rho(\overline{r}) = \rho_0(\overline{r})$. These two theorems only state that such a functional $E[\rho]$ exists with the variational property given by Eq. (2.16). In the following year Kohn and Sham [63] provided a procedure by which we can approximate the functional and hence solve for the ground state energy and density. They decomposed the energy functional as the sum of three components:

$$E[\rho] = T_0[\rho] + U[\rho] + E_{xc}[\rho] \tag{2.18}$$

The first term is the kinetic energy of electrons in a system which has the same density $\rho(\overline{r})$ as the real system but in which the electrons are assumed to be *non-interacting* with the electron-electron interactions turned off. The second term comprises the sum of the usual Hartree Coulomb energy and the electrostatic interaction energy between the electrons and the external potential due to the nuclei i.e.

$$U[\rho] = \int [\hat{U}_H(\overline{(r)} + \hat{U}_{ext}(\overline{r})]\rho(\overline{r})d\overline{r} \tag{2.19}$$

$$\hat{U}_H[\overline{r}] = \int \frac{\rho(\overline{r}')}{|\overline{r}' - \overline{r}|}d\overline{r}' \tag{2.20}$$

$$\hat{U}_{ext}[\rho] = -\sum_{\alpha} \frac{Z_\alpha}{|\overline{r} - \overline{R}_\alpha|} \tag{2.21}$$

The third term is the so-called exchange-correlation energy functional, that comprises the sum of the Hartree-Fock exchange energy plus the correlation energy that remains to make the functional Eq. (2.18) exact.

Thomas-Fermi theory [59, 60] had assumed that the non-interacting kinetic energy functional for an *inhomogeneous* system could be approximated by using the kinetic energy density of a homogeneous free electron gas corresponding to the density $\rho(\overline{r})$ at each point in space, namely

$$T_0^{TF}[\rho] = A_s \int \rho(\overline{r})^{\frac{5}{3}} d\overline{r} \tag{2.22}$$

where $A_s = \frac{3}{10}(3\pi^2)^{\frac{2}{3}} = 2.871$ atomic units. This approximation failed to describe chemical bonding correctly. Kohn and Sham took the key step of defining the non-interacting kinetic energy functional in the spirit of the original Schrödinger equation (2.1), namely

$$T_0[\rho] = \sum_i n_i \int \psi_i^*(\overline{r})[-\frac{1}{2}\nabla^2]\psi_i(\overline{r}) d\overline{r} \tag{2.23}$$

where n_i is the occupation number of state i and $\psi_i(\overline{r})$ is an orthonormal set of single-particle wave functions such that

$$\rho(\overline{r}) = \sum_{i=1}^{N} |\psi_i(\overline{r})|^2 \tag{2.24}$$

The ground state energy is found by minimizing the energy $E[\rho]$ in Eq. (2.18) with respect to variations in the electron density $\rho(\overline{r})$, given by Eq. (2.24), subject

to the constraint that the number of particles is conserved through Eq. (2.17). Using variational calculus it may be shown [63] that the ground state energy can be written

$$E[\rho] = \sum_{i=1}^{N} \epsilon_i - \frac{1}{2} \int \int \frac{\rho(\overline{r})\rho(\overline{r}')}{|\overline{r} - \overline{r}'|} d\overline{r} d\overline{r}' - \int \hat{U}_{xc}(\overline{r})\rho(\overline{r}) dr + E_{xc}[\rho] \tag{2.25}$$

where

$$\hat{U}_{xc}(\overline{r}) = \frac{\delta E_{xc}[\rho(\overline{r})]}{\delta \rho(\overline{r})} \tag{2.26}$$

The occupied energy levels ϵ_i that enter the sum in the first term of Eq. (2.25) are the eigenvalues resulting from solving a Schrödinger-like equation for non-interacting particles:

$$[-\frac{1}{2}\nabla^2 + \hat{U}_{eff}(\overline{r})]\psi_i(\overline{r}) = \epsilon_i \psi_i(\overline{r}) \tag{2.27}$$

where

$$\hat{U}_{eff}(\overline{r}) = \hat{U}_{ext}(\overline{r}) + \hat{U}_H(\overline{r}) + \hat{U}_{xc}(\overline{r}) \tag{2.28}$$

Thus, Kohn and Sham provided a recipe for solving the ground state energy of a many-body electron system within an effective one-electron framework provided the form of the exchange-correlation functional that enters both the Schrödinger equation (2.27) and the total energy (2.25) is known. This we now turn to in the next section.

2.4 The Exchange-Correlation Functional

Several different schemes have been developed for obtaining approximate forms for the functional for the exchange-correlation energy. The simplest and yet suprisingly accurate approximation, for non-magnetic systems is to assume that the exchange-

correlation energy is dependent only on the local electron density $\rho(\overline{r})$ around each volume element $d\overline{r}$. This is called the *local density approximation* (LDA). The local density approximation rests on two basic assumptions: firstly, the exchange and correlation effects come predominantly from the immediate vicinity of the point $\overline{r}$, and secondly these exchange and correlation effects do not depend strongly on the variations of the electron density in the vicinity of $\overline{r}$. If these two conditions are reasonably well fulfilled, then the contribution from the volume element $d\overline{r}$ would be the same as if this volume element were surrounded by a homogeneous electron density of the constant value $\rho(\overline{r})$ within $d\overline{r}$. Within LDA the exchange-correlation energy functional is given by:

$$E_{xc}^{LDA}[\rho] = \int \rho(\overline{r})\varepsilon_{xc}[\rho(\overline{r})]d\overline{r} \tag{2.29}$$

where $\varepsilon_{xc}(\rho(\overline{r}))$ is the exchange-correlation energy per particle of a uniform electron gas. This quantity is split into two parts:

$$\varepsilon_{xc}(\rho(\overline{r})) = \varepsilon_x(\rho(\overline{r})) + \varepsilon_c(\rho(\overline{r})) \tag{2.30}$$

The exchange part $\varepsilon_x(\rho(\overline{r}))$ can be derived analytically within the Hartree-Fock approximation and can be expressed as

$$\varepsilon_x(\rho(\overline{r})) = -\frac{3}{4}\sqrt[3]{\frac{3\rho(\overline{r})}{\pi}} \tag{2.31}$$

The correlation part cannot be derived analytically, but can be calculated numerically with high accuracy by means of Monte Carlo simulations [64].

The LDA is generally very successful in predicting structures and ground state properties of materials but some shortcomings are well documented [65]. These concern in particular: (i) the energies of excited states, in particular the band gaps in semiconductors and insulators are systematically underestimated. This is not suprising since DFT is based on a theorem referring to the ground state only. (ii) Generally, LDA tends to significantly overestimate cohesive energies and underestimate lattice parameters by up to 3%. In solids, the former is thought to occur because the LDA does a poor calculation of the total energy in isolated atoms [66]. (iii) The incorrect ground state is predicted for some magnetic systems (the most notable example is Fe which is predicted to be hexagonal close packed and non-magnetic instead of body-centered cubic and ferromagnetic) and for strongly correlated systems (e.g. the Mott insulators NiO and La_2CuO_4 are predicted to be metallic in the LDA). (iv) Van der Waals interactions are not appropriately described in the LDA, although there are some recent suggestions for overcoming this problem [67, 68]. In magnetic systems or in systems where open electronic shells are involved, the *local spin density approximation* (LSDA) which is the equivalent of the LDA in spin-polarized systems is employed. LSDA basically consists of replacing the exchange-correlation energy density with a spin-polarized expression [61].

During recent years several schemes that go under the generic name of the *generalized-gradient approximation* (GGA) attempt to provide improvements to LDA by expanding $E_{xc}[\rho]$. The expansion is not a simple Taylor expansion, but tries to find the correct asymptotic behaviour and correct scaling for the usually nonlinear expansion. These enhanced functionals are frequently called nonlocal or gradient corrections, since they depend not only upon density, but also the magnitude of the gradient of the density at a given point. For materials applications, the GGAs proposed by Perdew and co-workers [66, 69, 70, 71, 72], have been widely used and have proved to be quite successful in correcting some of the deficiencies of the LDA: the overbinding being largely corrected (the GGAs lead to larger lattice constants and lower cohesive energies) [73] and the correct magnetic ground state is predicted for ferromagnetic Fe [74] and antiferromagnetic Cr and Mn [75]. However, there are also cases where the GGA overcorrects the deficiencies of the LDA and leads to a large underbinding [65].

The basic idea of GGAs is to express the exchange-correlation energy in the following form:

$$E_{xc}^{GGA}[\rho] = \int \rho(\overline{r})\varepsilon_{xc}[\rho(\overline{r})]d\overline{r} + \int F_{xc}[\rho(\overline{r}), \nabla\rho(\overline{r})]d\overline{r} \tag{2.32}$$

where the function F_{xc} is asked to satisfy a number of formal conditions for the exchange-correlation hole, such as sum rules, long-range decay and so on. Naturally,

not all the formal properties can be enforced at the same time, and this differentiates one functional from another [61].

The form suggested by Becke [70] for the exchange part is:

$$E_x^{GGA}[\rho_\uparrow, \rho_\downarrow] = E_x^{LDA} - \beta \sum_\sigma \int \frac{\rho_\sigma(\overline{r})^{\frac{4}{3}} x_\sigma^2}{1 + 6\beta x_\sigma \sinh^{-1} x_\sigma} d^3\overline{r} \tag{2.33}$$

where

$$E_x^{LDA} = -C_x \sum_\sigma \int \rho_\sigma^{\frac{4}{3}}(\overline{r}) d^3\overline{r}, \tag{2.34}$$

$C_x = \frac{3}{2}\left(\frac{3}{4\pi}\right)^{\frac{1}{3}}$, $x_\sigma = |\nabla\rho_\sigma| / \rho_\sigma^{4/3}$ and σ denotes either $\uparrow$ or $\downarrow$ electron spin. The constant β is a parameter fitted to obtain the correct exchange energy of noble gas atoms. The GGA improves predicted values of binding and dissociation energies and brings them to within 10 kJ/mol (about 1.0 eV) of experiment [69].

The following correlation functional as proposed by Perdew and Wang [69] predicts correlation energies of useful accuracy for an electron gas with slowly varying density:

$$E_c^{GGA}[\rho_\uparrow, \rho_\downarrow] = \int \rho(\overline{r}) \varepsilon_c(\rho_\uparrow, \rho_\downarrow) d^3\overline{r} + \int \frac{C_c(\rho) |\nabla\rho(\overline{r})|^2}{d e^\Phi \rho(\overline{r})^{4/3}} d^3\overline{r} \tag{2.35}$$

where

$$d = 2^{\frac{1}{3}} \left[\left(\frac{1+\zeta}{2}\right)^{\frac{5}{3}} + \left(\frac{1-\zeta}{2}\right)^{\frac{5}{3}} \right]^{\frac{1}{2}}, \tag{2.36}$$

$$\Phi = 0.1929 \left[\frac{C_c(\infty)}{C_c(\rho)}\right] \frac{|\nabla\rho|}{\rho^{7/6}}, \tag{2.37}$$

$\zeta = (\rho_\uparrow - \rho_\downarrow)/\rho$ and $C_c(\rho)$ is a rational polynomial of the density that contains seven fitting parameters.

The correlation energy per particle of the uniform electron gas, $\varepsilon_c(\rho_\uparrow, \rho_\downarrow)$, is taken from a parametrization by Perdew and Zunger [76] of the Ceperly-Alder [77] Monte Carlo results.

In this thesis we have used the most recent form of GGA due to Perdew-Burke-Ernzerhof (PBE) [72, 78]. They write the exchange functional in a form which contains an explicit enhancement factor F_x over the local exchange, namely:

$$E_x^{PBE}[\rho_\uparrow, \rho_\downarrow] = \int \rho(\overline{r})\varepsilon_x^{LDA}[\rho(\overline{r})]F_{xc}(\rho, \xi, s)d\overline{r} \tag{2.38}$$

where ρ is the local density, ξ is the relative spin polarization, and $s = |\nabla\rho(\overline{r})|/(2k_F\rho)$ is the dimensionless density gradient. Following [43] the enhancement factor is written

$$\left(sF_x = \frac{1}{\kappa + s^2\mu}\left(\kappa + s^2\mu + s^2\kappa\mu\right)\right) \tag{2.39}$$

where $\mu = \beta(\pi^2/3) = 0.21951$ with $\beta = 0.066725$ being related to the second-order gradient expansion [71]. This form was chosen because it

(i) satisfies the uniform scaling condition,

(ii) recovers the correct uniform electron gas limit because $F_x(0) = 1$,

(iii) obeys the spin-scaling relationship,

(iv) recovers the local spin density approximation (LSDA) linear response limit for $s \longrightarrow 0$, namely $F_x(s) \longrightarrow 1 + \mu s^2$, and

(v) satisfies the local Lieb-Oxford bound [79], $\varepsilon_x(\overline{r}) \geq -1.679\rho(\overline{r})^{4/3}$, that is, $F_x(s) \leq 1.804$, for all $\overline{r}$, provided that $\kappa \leq 0.804$. PBE chooses the largest allowed value, $\kappa = 0.804$.

The correlation energy on the otherhand is written in the form:

$$E_c^{PBE}[\rho_\uparrow, \rho_\downarrow] = \int \rho(\overline{r}) \left[\varepsilon_c^{LDA}(\rho, \zeta) + H[\rho, \zeta, t]\right] d\overline{r} \tag{2.40}$$

with

$$H[\rho, \zeta, t] = \gamma\phi^3 In \left\{1 + \frac{\beta\gamma^2}{t}[\frac{1 + At^2}{1 + At^2 + A^2t^4}]\right\} \tag{2.41}$$

Here, $t = |\nabla\rho(\overline{r})| / (2\phi k_s\rho)$ is a dimensionless density gradient, $k_s = (4k_F/\pi)^{1/2}$ is the TF screening wave number and $\phi(\zeta) = \left[(1+\zeta)^{2/3} + (1-\zeta)^{2/3}\right]/2$ is a spin-scaling factor. The quantity β is the same for the exchange term $\beta = 0.066725$, and $\gamma = 0.031091$. The function A has the following form:

$$A = \frac{\beta}{\gamma}\left[e^{-\varepsilon_c^{LDA}\frac{[\rho]}{\gamma\phi^3}} - 1\right]^{-1} \tag{2.42}$$

So defined, the correlation term H satisfies the following properties [61]:

(i) it tends to the correct second-order gradient expansion in the slowly varying (high-density) limit ($t \longrightarrow 0$),

(ii) it approaches minus the uniform electron gas correlation $-\varepsilon_c^{LDA}$ for rapidly varying densities ($t \longrightarrow \infty$), thus making the correlation energy vanish (this results from the correlation hole sum rule), and

(iii) it cancels the logarithmic singularity of ε_c^{LDA} in the high-density limit, thus forcing the correlation energy to scale to a constant under uniform scaling of the density.

We will see in chapter 4 that this PBE exchange-correlation gives good results for the Mg-Li alloy system.

Chapter 3
PLANE WAVE PSEUDOPOTENTIAL METHOD

In this chapter we outline the methodology of solving the Kohn-Sham equation, Eq. (2.27), using a plane wave basis and approximating the ion cores with pseudopotentials. We will end with a brief discussion of the commercial software package CASTEP that will be used in subsequent chapter.

3.1 Plane Wave Basis Sets

The plane-wave pseudopotential (PWP) method begins by representing the system by a 3-dimensional periodic supercell. This allows Bloch's theorem to simplify the task of solving the Kohn-Sham equation. This is because Bloch's theorem which is based upon the periodicity of the system, reduces the infinite number of one-electron wavefunctions in the real system to only the number of electrons in the chosen supercell. Following Bloch's theorem, the wavefunction can be written as the product of a cell periodic part and a wavelike part:

$$\psi_i(\overline{r}) = \exp(i\overline{k} \cdot \overline{r}) f_i(\overline{r}). \tag{3.1}$$

The first term is the wavelike part and the second term is the cell periodic part of the wavefunction, which can be expressed by expanding it into a finite number of planewaves whose wave vectors are the reciprocal lattice vectors of the crystal,

$$f_i(\overline{r}) = \sum_{\overline{G}} c_{i,\overline{G}} \exp(i\overline{G} \cdot \overline{r}) \tag{3.2}$$

where $\overline{G}$ are the reciprocal lattice vectors. Therefore each electronic wavefunction is written as a sum of plane waves,

$$\psi_i(\overline{r}) = \sum_{\overline{G}} c_{i,\overline{k}+\overline{G}} \exp[i(\overline{k} + \overline{G}) \cdot \overline{r}]. \tag{3.3}$$

The problem of solving the Kohn-Sham equation has now been mapped onto the problem of expressing the wavefunction in terms of an infinite number of reciprocal space vectors for each point **k** within the first Brillouin zone of the periodic cell. For metallic systems a dense set of **k** points is required to define the Fermi surface precisely and to reduce the magnitude of the error in the total energy which may arise due to inadequacy of the **k**-point sampling. We will see later in chapter 4 that the computed total energy converges as the density of **k** points increases so that the error due to the **k**-point sampling can be made as small as needed. In principle, a converged electronic potential and total energy can always be obtained provided that the computational time and memory are available to calculate the electronic wave functions at a sufficiently dense set of **k** points [25].

The Fourier series in Eq. (3.3) is, in principle, infinite. However, the coefficients $c_{i,\overline{k}+\overline{G}}$ are associated with plane waves of kinetic energy $(\hbar^2/2m)\left|\overline{k}+\overline{G}\right|^2$. The plane waves with a smaller kinetic energy typically play a more important role than those with a very high kinetic energy. The introduction of a plane wave energy cutoff reduces the basis set to a finite size. This kinetic energy cutoff will lead to an error in the total energy of the system but in principle it is possible to make this error arbitrarily small by increasing the size of the basis set by allowing a larger energy cutoff. In principle, the cutoff energy should be increased until the calculated total energy converges within the required tolerance [25]. We will see later in chapter 4 that this is essential for the phase stability study of Mg-Li alloys where the absolute values of the total energies of different structures are compared.

The main advantage of expanding the electronic wavefunctions in terms of a basis set of plane waves is that the Kohn-Sham equation take a particularly simple form. Substitution of Equation 3.3 into the Kohn-Sham equation, (2.27), gives

$$\sum_{\overline{G}'}\{\frac{\hbar^2}{2m}\left|\overline{k}+\overline{G}\right|^2\delta_{\overline{G}\overline{G}'}+U_{ext}(\overline{G}-\overline{G}')+U_H(\overline{G}-\overline{G}')+U_{xc}(\overline{G}-\overline{G}')\}c_{i,\overline{k}+\overline{G}'}=\varepsilon_i c_{i,\overline{k}+\overline{G}'}\,. \tag{3.4}$$

We see immediately that the reciprocal space representation of the kinetic energy is diagonal with the various potential contributions being described in terms of their Fourier components. The usual method of solving the plane wave expansion of the Kohn-Sham equation is by diagonalisation of the Hamiltonian matrix whose el-

ements $H_{\overline{k}+\overline{G},\overline{k}+\overline{G}'}$, are given by the terms in curly brackets above. The size of the matrix is determined by the choice of cutoff energy

$$E_c = \frac{\hbar^2}{2m}\left|\overline{k}+\overline{G}_c\right|^2 \tag{3.5}$$

and will be intractably large for systems that contain both valence and core electrons. This classical problem was solved by advent of the powerful concept of pseudopotentials.

3.2 Pseudopotential Approximation

The fundamental idea of pseudopotentials is to replace the real potential, arising from the nuclear charge and the core electrons, with an effective potential, within a core region of radius R_c, as illustrated schematically in Figure 3.1. Certain demands are then placed on this effective potential. It must be such that the valence orbital eigenvalues are the same as those in an all-electron calculation on the atom. It must also preserve the continuity of the wavefunctions and their first derivatives across the core boundary. Finally, integrating the charge in the core region should give the same answer for the pseudo-atom and the all-electron one, that is, the pseudopotential must be *norm-conserving*. A pseudopotential that satisfies these demands will have the same scattering properties, at energies corresponding to valence eigenvalues, as the ionic core it replaces. The self-consistent field equations (Eqs. 2.24 and 2.27) are carried out only for the valence electrons. Moreover, since the core electrons which

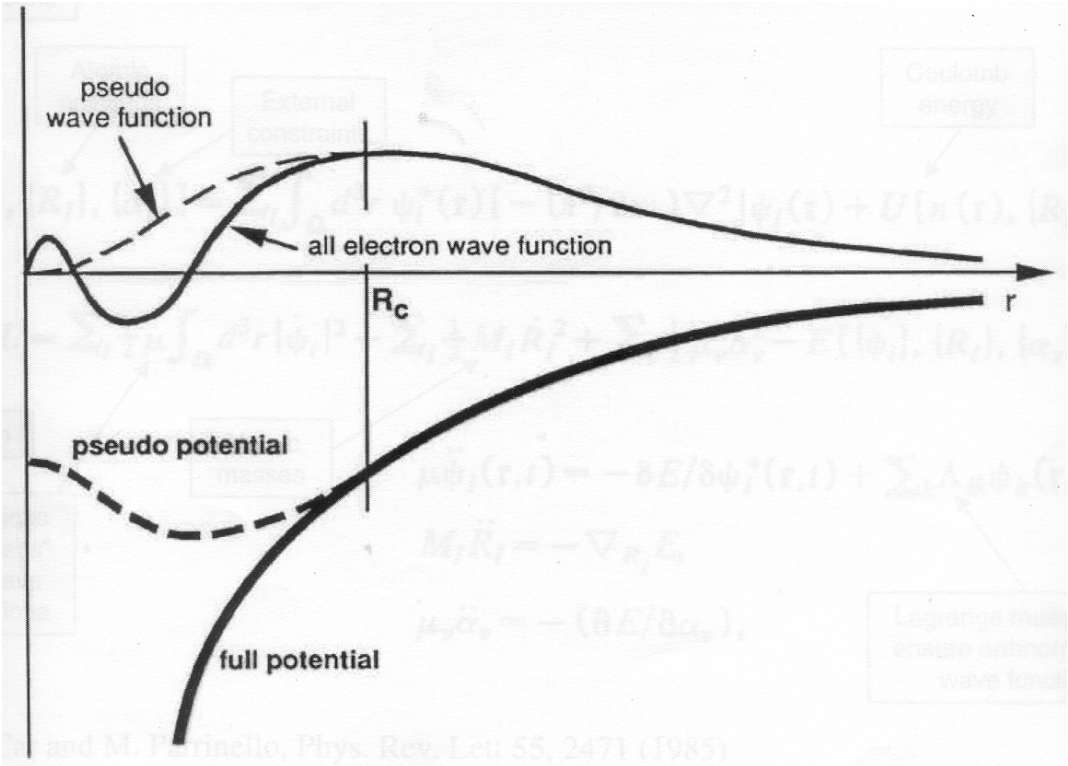

Figure 3.1: Schematic illustration of all-electron (solid lines) and pseudoelectron (dashed lines) potentials and their corresponding wave functions. The radius at which all-electron and pseudoelectron values match is designated $\mathbf{R}_c$ [25].

do not influence the properties of the solid phase are removed from the problem, much higher numerical precisions can be achieved. Thus, systems involving heavy atoms are not much more complicated than those with light ones.

The phase shift produced by the ionic core is different for each angular momentum component (s, p, d, etc.) of the valence wavefunction. Thus, the scattering from the pseudopotential must be angular momentum dependent. The most general form for a pseudopotential is:

$$V_{NL} = \sum |l_m\rangle V_l \langle l_m| \tag{3.6}$$

where $\mid l_m\rangle$ are spherical harmonics and V_l is the pseudopotential for angular momentum l [90]. A pseudopotential that uses the same potential in each angular momentum channel is called a local pseudopotential. Local pseudopotentials are computationally much more efficient than nonlocal ones. However, only a few elements such as aluminium can be described accurately using local pseudopotentials. Lithium, in particular, requires a careful non-local treatment due to the absence of any *p* states in its ion core.

An important recent concept in pseudopotential applications is the degree of *hardness* of a pseudopotential. A pseudopotential is considered *soft* when it requires a small number of Fourier components for its accurate representation and *hard* otherwise. Norm conservation ensures the scattering properties remain correct away from the eigenvalues to linear order in the energy [91] and also ensures that the pseudo-wavefunction matches the all-electron wavefunction beyond a cutoff radius that defines the core region. Within the core region, the pseudo wavefunction has no nodes and is related to the all-electron wavefunction by the *norm-conservation*: that is, both wavefunctions carry the same charge. These potentials can be made very accurate at the price of having to use a very high energy cutoff. Early development of accurate norm-conserving pseudopotentials quickly showed that the potentials for the first row elements such as Li turn out to be extremely *hard* [41]. Various schemes have been

suggested to improve convergence properties of norm-conserving pseudopotentials [92].

Despite the best attempts to optimize their performance for the first row elements [93, 94], a more radical approach was required, as suggested by Vanderbilt [95]. This involves relaxing the norm-conserving requirement in order to generate much *softer* pseudopotentials, *ultrasoft pseudopotentials* (USP). In the ultrasoft pseudopotential scheme, the pseudo-wave-functions are allowed to be as *soft* as possible within the core region, so that the cutoff energy can be reduced dramatically. USP have another advantage besides being much *softer* than their norm-conserving counterparts. The generation algorithm guarantees good scattering properties over a pre-specified energy range, which results in much better transferability and accuracy of the pseudopotentials. This leads to high accuracy and transferability of the potentials, although at a price of computational efficiency. Typically it is found that E_c is about half that for a norm-conserving pseudopotential, which means less than one-third as many plane waves are required. In chapter 4 the Mg-Li alloys are modelled with Vanderbilt ultrasoft pseudopotentials.

3.3 Grids and Fast-Fourier transforms

Real- and reciprocal-space grids are another key feature of the PWP method. Expressing the wavefunction as an expansion in a finite set of plane waves leads naturally to the idea of a reciprocal-space grid. However, it is advantageous to have a

real-space representation too, on the related real-space grid [96]. Fast Fourier transforms (FFT's) are used to transform the data between the two spaces in a highly efficient manner. The direct lattice vectors of the real-space supercell are denoted $\overline{a}_1, \overline{a}_2$ and $\overline{a}_3$. The reciprocal lattice vectors $\overline{b}_i$ are defined by the relation $\overline{a}_i \cdot \overline{b}_j = 2\pi\delta_{ij}$, where $\delta_{ij} = 1$ for $i = j$ but zero otherwise. In practice $\overline{b}_i$ is constructed using

$$\overline{b}_1 = \overline{a}_2 \times \overline{a}_3/(\overline{a}_1 \cdot \overline{a}_2 \times \overline{a}_3), \tag{3.7}$$

$$\overline{b}_2 = \overline{a}_3 \times \overline{a}_1/(\overline{a}_1 \cdot \overline{a}_2 \times \overline{a}_3), \tag{3.8}$$

$$\overline{b}_3 = \overline{a}_1 \times \overline{a}_2/(\overline{a}_1 \cdot \overline{a}_2 \times \overline{a}_3). \tag{3.9}$$

A reciprocal lattice vector $\overline{G}$ is given by

$$\overline{G} = n_1\overline{b}_1 + n_2\overline{b}_2 + n_3\overline{b}_3 \tag{3.10}$$

where n_i are integers . A plane wave $\exp(i\overline{G} \cdot \overline{r})$ is commensurate with the supercell, and the set plane waves whose wavevectors are defined by equation 3.10 above is an orthogonal set [96]. The real-space grid is formed by dividing the lattice vectors $\overline{a}_1, \overline{a}_2$ and $\overline{a}_3$ into N_1, N_2 and N_3 points. A point in the supercell is then denoted

$$(l_1, l_2, l_3)\overline{r} = \frac{l_1}{N_1}\overline{a}_1 + \frac{l_2}{N_2}\overline{a}_2 + \frac{l_3}{N_3}\overline{a}_3, \tag{3.11}$$

where the l_i are integers in the range $0 \leq l_i \leq (N_i - 1)$. The real-space grid can be viewed as the lattice of points for the lattice vectors $\alpha_i = \overline{a}_i/N_i$. The corresponding reciprocal lattice vectors are given by $\beta_i = N_i\overline{b}_i$ because of the relation $\alpha_i \cdot \beta_j = 2\pi\delta_{ij}$. The vectors β_i are the reciprocal-space supercell vectors. The reciprocal-space grid is the lattice of points for the vectors $\overline{b}_i$. Within the reciprocal-space supercell a point is given by equation 3.10 with $0 \leq n_i \leq (N_i - 1)$. In each supercell there are $N_1N_2N_3 = N$ points. It can be said that discrete Fourier transforms, or at least plane waves, impose these relationships between the grids. The products $\overline{G} \cdot \overline{r}$ are independent of the supercell dimensions.

Although pseudopotentials have reduced the number of plane waves required, that number is still large. FFT's play a role of equal importance because they allow the calculation to scale well with system size.

3.4 Broadening (smearing) scheme

In *ab initio* electronic structure and total-energy calculations the integrals over the Brillouin zone are commonly replaced by the sum over a mesh of **k**-points. This approach is very efficient for insulators, but for metallic systems convergence with respect to the number of **k**-points becomes slow. The introduction of fractional occupation numbers is a convenient way to improve the **k**-space integration and in addition to stabilize the convergence in the iterative approach to self-consistency [97]. In these broadening schemes the eigenstates are occupied according to a gaussian-

like smearing of each energy level. The remaining task is to effectively convert these eigenvalues into an electronic density of states $n(E)$. The Fermi level, E_F, can then be found from the electron count

$$N = \int dE n(E)\theta(E_F - E), \tag{3.12}$$

after which the band energy can be determined:

$$E_{band} = \int dE E n(E)\theta(E_F - E) = E_0. \tag{3.13}$$

In an insulator the approximation to E_{band} improves monotonically as the number of k-points is increased, whilst for metals the process breaks down as the Fermi level is in the middle of an occupied band. Accurately determining Eq. 3.13 then requires an extremely large number of k-points.

It has long been recognized that this problem can be alleviated by ‘smearing‘ the step function $\theta(E_F - E)$ into a smooth weighting function $f_T(E)$ [83]. Gillan [98] provided a formal basis for this technique, beginning from the observation that the Fermi-Dirac function

$$f_T(E) = 1/\{1 + \exp[(E - \mu(T))/T]\} \tag{3.14}$$

is the weighting function which minimizes the free energy

$$A_{band}(T) = E_{band}(T) - TS(T), \tag{3.15}$$

where T is a fictitious "temperature", the chemical potential $\mu(T)$ approaches E_F as $T \rightarrow 0$, and S is the associated entropy

$$S(T) = \int dEn(E)\{f_T(E)Inf_T(E) + [1 - f_T(E)]In[1 - f_T(E)]\}. \quad (3.16)$$

Now E_{band} is also an explicit function of T

$$E_{band}(T) = \int dEEn(E)f_T(E). \quad (3.17)$$

Gillan then showed that at low temperatures

$$E_{band}(T) = E_0 \pm \frac{1}{2}\gamma T^2 + O[T^n], \quad (3.18)$$

$$A_{band}(T) = E_0 \pm \frac{1}{2}\gamma T^2 + O[T^n]. \quad (3.19)$$

Later, Grotheer and Fähnle [99] showed that $n \geq 4$. From this they deduced that

$$U(T) = [E_{band}(T) + A_{band}(T)]/2 = E_0 + O[T^4]. \quad (3.20)$$

The T^4 dependence of the correction to the ground-state energy should allow one to use a relatively large broadening temperature and extrapolate back to $T = 0$ via Eq. 3.20. Since T is large, the integrand of Eq. 3.17 cuts off smoothly with increasing energy, decreasing the number of k-points needed to provide an accurate energy. Broadening methods, using either Eq. 3.14 or some other weighting function

[99] which satisfies Eq. 3.20, have been widely used in most recent articles in *Physical Review B* since 1998. In these papers the value of the broadening "temperature" or equivalent ranges from 2 mRy [100] to 20 mRy [101]. Only one paper [97] gives any justification for the choice of a particular temperature.

3.5 Advantages of PWP method

The PWP approach has several advantages over other methods, such as those based on localized atomic orbitals. These are:

(i) convergence with respect to the completeness of the basis set is easily checked by extending the cut-off energy (i.e. the highest kinetic energy in the PW basis),

(ii) Fast-Fourier-Transforms (FFT) facilitate the solution of the Poisson equation, and

(iii) forces on atoms and stresses on the unit cell may be calculated directly via the Hellmann-Feynman [102] theorem, without applying Pulay corrections for the site-dependence of the basis set [103].

The main disadvantage is that the chemical insights gained by a description of bonding between localized orbitals is not immediately apparent. However, new codes remove this deficiency by transforming from the PW description to a localized orbital description once the PWP calculations have converged to the relaxed ground state structure.

3.6 CASTEP code

The planewave pseudopotential (PWP) calculations for the solution of the Kohn-Sham equation of Density Functional Theory (DFT) were performed using CASTEP (Cambridge Serial Total Energy Package) [26] with the generalized gradient approximation for the exchange correlation energy functional. CASTEP is a pseudopotential total-energy code which employs special point integration over the Brillouin zone and a plane wave basis for the expansion of the wavefunctions. We used the PBE form of the GGA [72], which was designed to be more robust and accurate than the original GGA formulation. The total-energy code used, CASTEP, performs a variational solution to the Kohn-Sham equations by using a density mixing scheme [73] to minimize the total energy and also conjugate gradients to relax the ions under the influence of the Hellmann-Feynman forces.

CASTEP uses fast fourier transforms (FFT) to provide an efficient way of transforming various entities (wavefunctions, potentials) from real to reciprocal space and back as well as to reduce the computational cost and memory requirement for operating with the Hamiltonian on the electronic wave functions, a planewave basis for the expansion of the wavefunctions. The convergence of this expansion is controlled by a single parameter, namely the highest frequency at which the series is terminated (conventionally defined as the highest kinetic energy of a plane wave). In this work the summation over the Brillouin zone has been performed with weighted summation over wave vectors generated by Monkhorst-Pack scheme [104], which produces

a uniform mesh of **k** points in reciprocal space. A BFGS-based minimization technique was used for performing geometry optimization, either at ambient conditions or under external stress [26]. The Pulay density of mixing scheme [25] with conjugate gradient solver is applied and pseudopotentials parametrized in the reciprocal space, as implemented in the CASTEP code. An updated iterative (due to the inverse Hessian) is based on the calculated stress tensor and atomic forces.

Ultrasoft pseudopotentials of Vanderbilt form [95] were utilized. The above methodology produces very "soft" pseudopotentials which drastically reduce the number of plane waves needed to achieve convergence of the calculated properties. The pseudopotentials were generated using the PBE exchange correlation functional. We used convergence criterion of less than 2 x 10^{-5} eV on total energy change per atom, 10^{-3} Å on the displacement of atoms, 0.05 eVÅ^{-1} on the residual forces and 0.1 GPa on the residual bulk stress.

Chapter 4
THEORY OF PRACTICAL RESULTS

4.1 Introduction

The phase diagram of Mg-Li, which is shown in Figure 1.1, is determined by the free energies of the different competing phases [105]. In particular, above room temperature we find the hcp and bcc phases centered on the magnesium and lithium rich ends of the phase diagram respectively. We see that whereas we have only about 15 at% solubility of Li into Mg, we have about 70% solubility of Mg into Li. At concentrations around 50%, the bcc phase remains stable even at very low temperatures, although local short range ordering of B2 (CsCl) type has been observed [106, 107]. A metastable fcc phase has been found after cold working alloys with from 13.4 to 19.7 at% Mg [7, 107].

Hafner [31] in a seminal paper 30 years ago predicted the variation of the heats of formation of *disordered* bcc, hcp and fcc phases using second-order perturbation theory within the nearly-free-electron model. He successfully accounted for the metastability of the observed fcc phase and the wide domain of bcc phase stability. In this thesis we examine *ordered* superstructures of Mg-Li alloys with respect to underlying fcc and bcc lattices using ab initio DFT. Although these low temperature ordered ground states have not been observed, our first principles data base could

be used in the future to fit a cluster expansion [18] and hence perform CVM [20] or Monte Carlo [19] simulations of the temperature and concentration dependence of the Mg-Li phase diagrams. In addition we will use DFT to predict the variation in the elastic moduli within these ordered superstructures and point out an interesting correlation between the tetragonal shear modulus and the relative stability of the corresponding fcc and bcc lattices.

In this chapter we, therefore, begin by presenting the ordered superstructures with respect to underlying fcc and bcc lattices of the Mg-Li alloys in which we are interested. This will then be followed by convergence tests on the choice of the energy cutoff that determines the number of plane waves, on **k**-point sampling, and on the smearing width (broadening "temperature") for phases that are very close in energy. The elasticity theory is summarized in the last part of this section.

4.2 The bcc- and fcc-based ordered structures

In this thesis we consider ordered structures with respect to fcc and bcc underlying lattices due to their promising potential in structural applications. In particular, we examine Mg-Li alloys with the stoichiometries 3:1 and 1:1 which preserve the cubic symmetry, as illustrated in Fig.4.1. In order to study small additions of Mg and Li to pure Li and Mg metals respectively, we also examine the 7:1 stoichiometry with respect to the fcc lattice and the 15:1 stoichiometry with respect to the bcc lattice. These two ordered lattices retain the cubic symmetry as can be seen in Fig.4.1. Thus,

we will discuss the energetics of the cubic fcc-based phases, $L1_2$ ($MgLi_3$, Mg_3Li, and ($MgLi_7$, Mg_7Li) and the cubic bcc-based phases B2 (MgLi), B32 (MgLi), DO_3 ($MgLi_3$), Mg_3Li) and ($MgLi_{15}$, $Mg_{15}Li$). In addition, we will examine the tetragonal $L1_0$ (MgLi) and DO_{22} ($MgLi_3$, Mg_3Li) phases.

4.3 Convergence tests

4.3.1 Cut-off energy

We show that obtaining converged total energies with respect to the energy cutoff is vital before attempting any structural predictions, since often we are looking at energy differences of the order of about $5\ meV/atom$. Single point energy calculations were performed (at the experimental lattice constant where available) for different kinetic energy cutoffs at various number of **k**-points within GGA-PBE. The method used was employed because of its robustness for metallic systems. In Figures 4.2 and 4.3, we show the plots of the total energy against kinetic energy cutoff, from which the energy cutoff employed in each structure was determined. We see that these curves are jagged for low cutoff energies but become smoother as the cutoff energy is increased. Thus the kinetic energy cut-off of $500\ eV$ was chosen as the energy differences were less than $5\ meV/atom$ at this point (as shown in Figures 4.2 and 4.3). The reason for the jagged appearance of the E-V curve is the discontinuous change in the number of plane waves used at that cut-off energy. We used ultrasoft

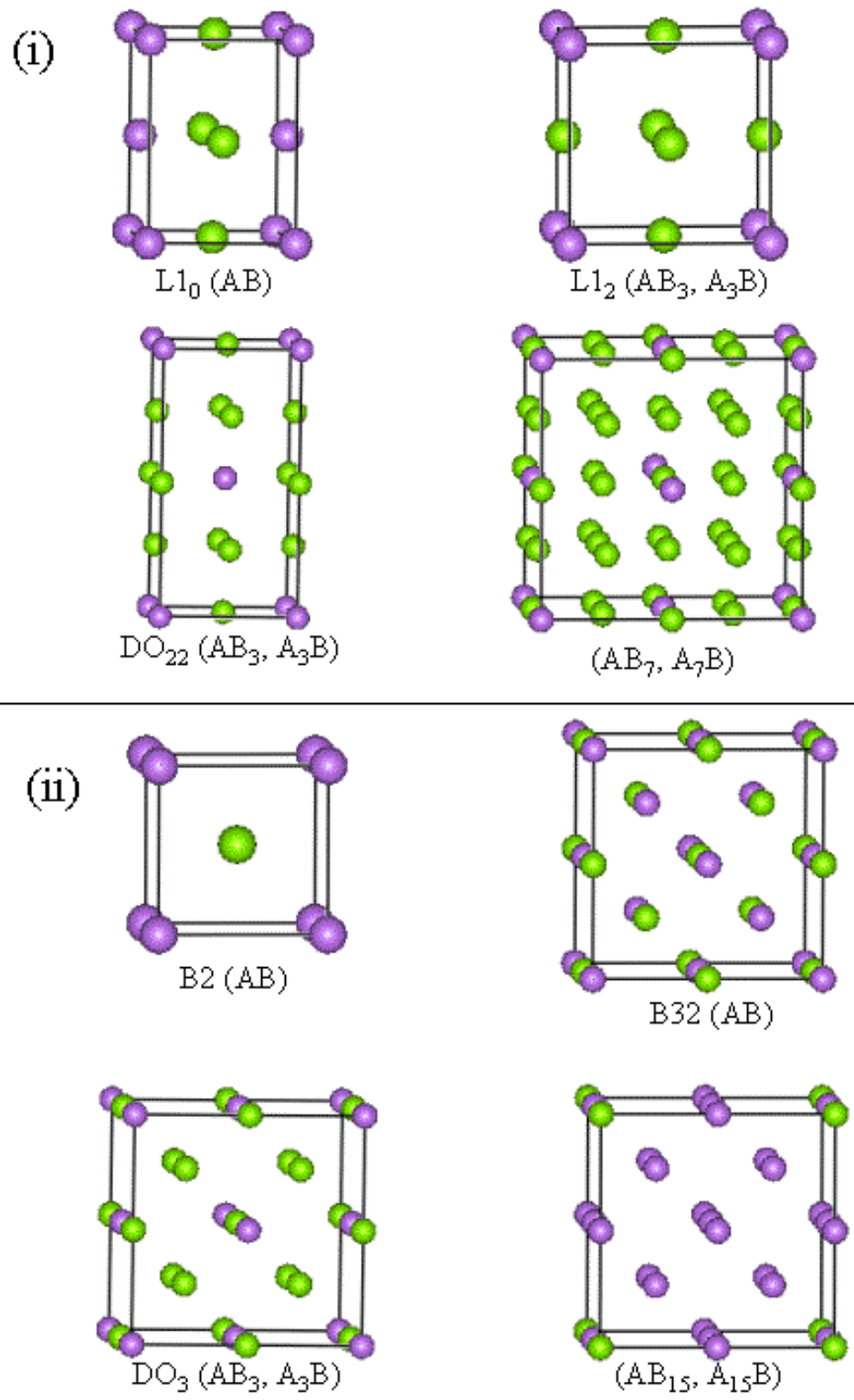

Figure 4.1: The ordered (i) fcc-based and (ii) bcc-based Mg-Li superstructures considered in this study.

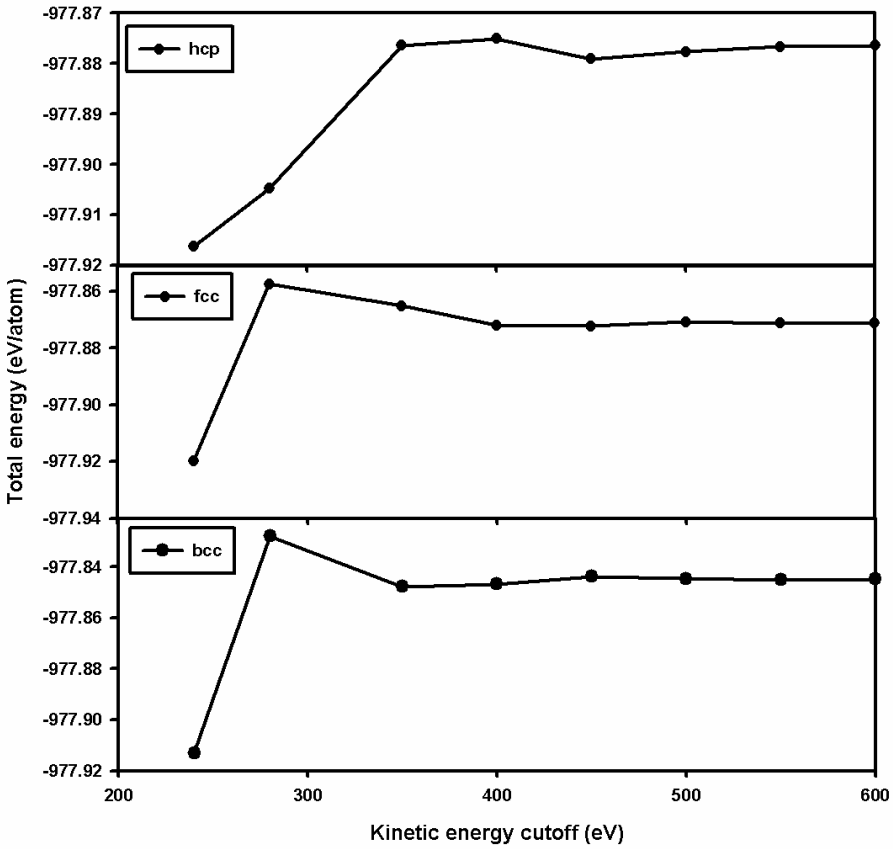

Figure 4.2: Plots of total energy against kinetic energy cut-off for Mg in hcp, fcc and bcc lattices.

pseudopotentials [95], which require significantly less computational resources than norm-conserving potentials [93].

4.3.2 k-points

Since we are comparing energies of different structures with different unit cell volumes and Brillouin shapes, sizes, and **k**-point sampling, we need a very good convergence of the energy. An appropriate choice of the **k**-point set is important for

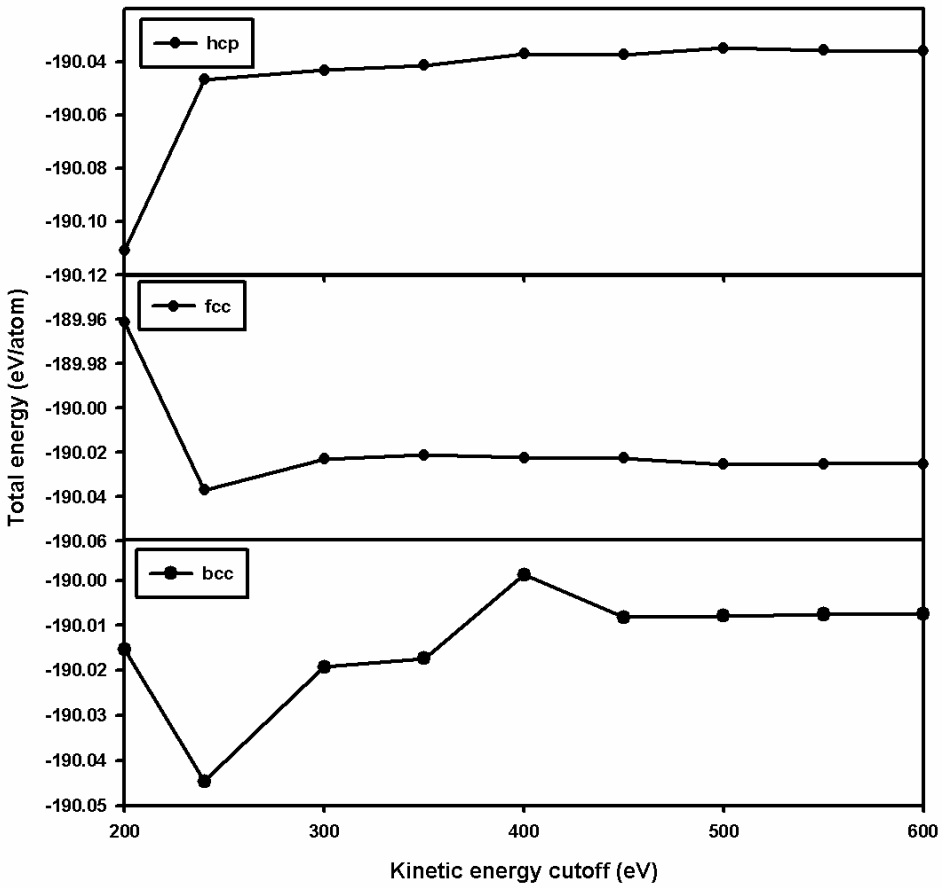

Figure 4.3: Plots of total energy against kinetic energy cut-off for Li in hcp, fcc and bcc lattices.

achieving balance between accuracy and efficiency. The Brillouin zone sampling was carried out using the number of **k** points as indicated in Table 4.1, within the irreducible part of the zone with the total in the full zone in brackets. This corresponds to the Monkhorst-Pack set of points given in the third column [104]. In this part, we show the convergence of the total energies with respect to the **k**-point sampling set size, as illustrated in the plots of total energy against number of **k**-points for Mg (Figure 4.4) and Li (Figure 4.5). The total energy was considered converged when the change was within $1\ meV$ and $5\ meV$ per atom for elemental metals and alloys respectively, and from this, **k**-points used were then chosen as listed in Table 4.1, since further increase of the **k**-point density had no significant effect on calculated properties. An increased **k**-point set reduces the finite basis set correction and makes cell relaxation more accurate at a fixed energy cutoff.

4.3.3 Smearing width

In CASTEP calculations for metallic systems, a Gaussian-like smearing width of each energy level, σ, is introduced to eliminate discontinuous changes in energy when an energy band crosses the Fermi level during the self-consistently procedure. This smearing width is set at a relatively large value, at first, to ensure convergence of our self-consistency procedure. When the procedure is converged then σ is decreased by halving in every six iterations until σ is no less than the specific minimum value. The values of the initial and final Gaussian-like smearing width of each energy level

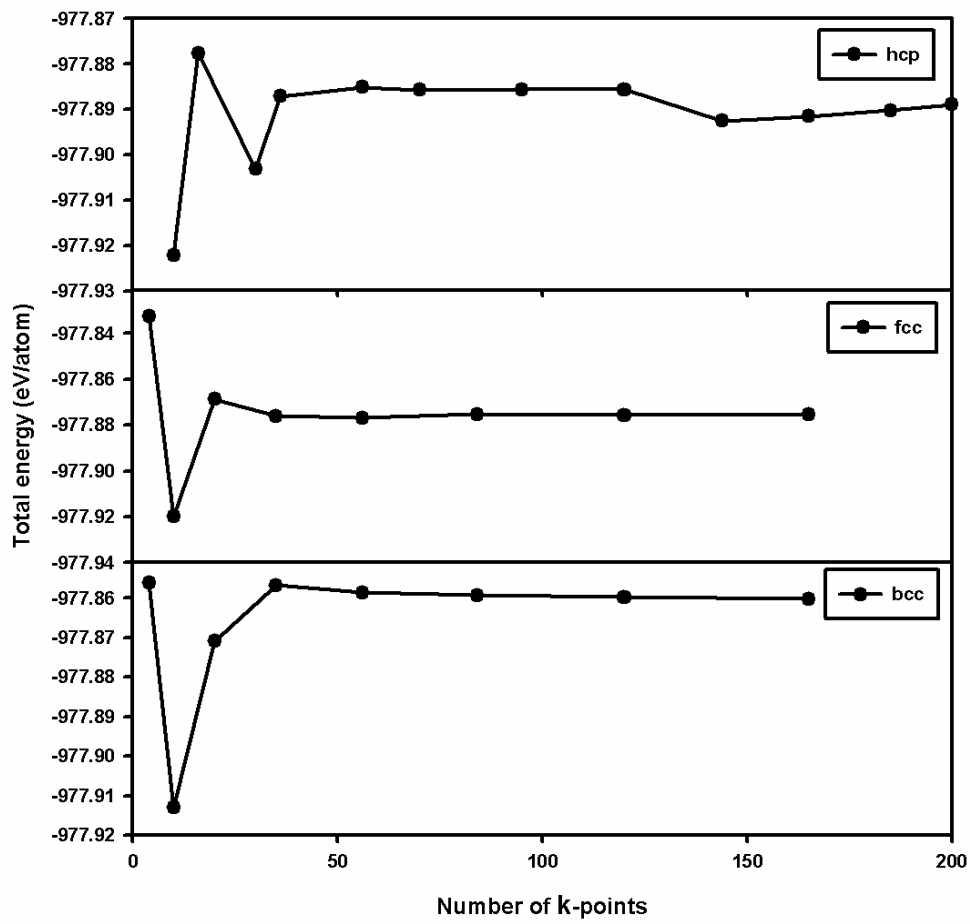

Figure 4.4: Plots of total energy versus number of **k**-points within the irreducible Brillouin zone for Mg in hcp, fcc and bcc lattices.

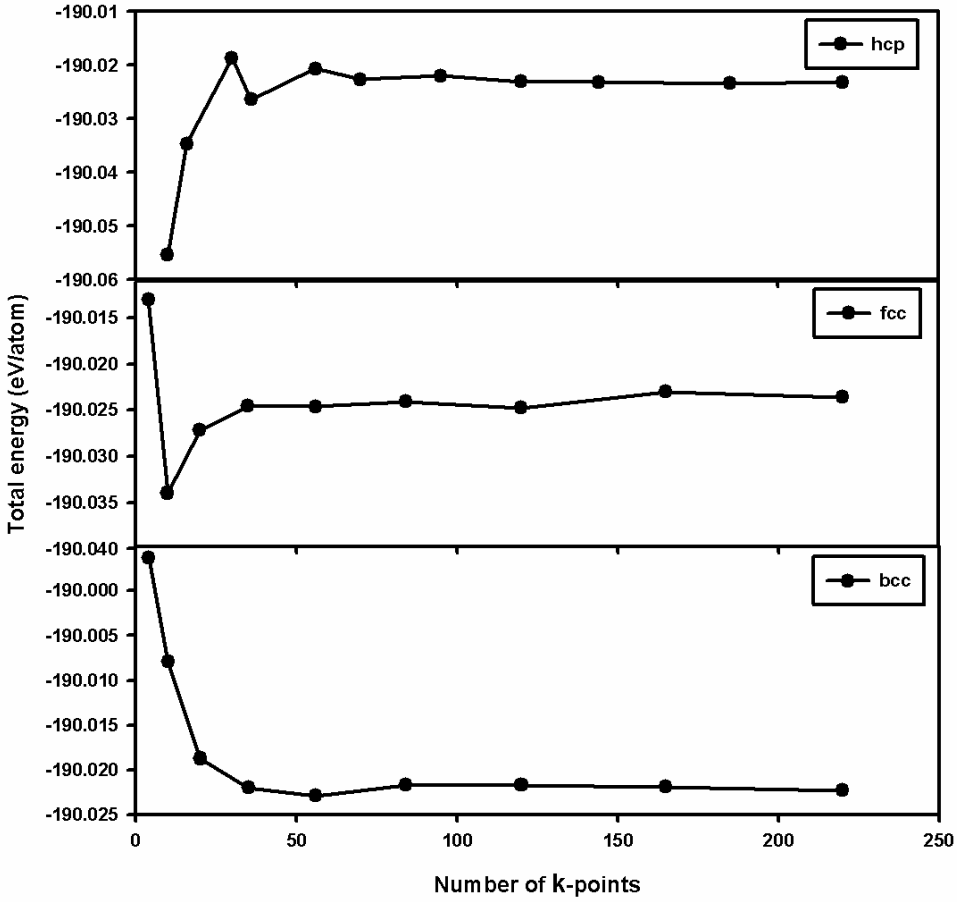

Figure 4.5: Plots of total energy against number of **k**-points within the irreducible Brillouin zone for Li in hcp, fcc and bcc lattices.

Structure	Number of **k**-points	Monkhorst-Pack set	No. of **k**-points x No. of atoms in unit cell
Mg (hcp)	96 (784)	14 x 14 x 8	192
Mg (fcc)	56 (864)	12 x 12 x 12	224
Mg (bcc)	56 (864)	12 x 12 x 12	112
$Mg_{15}Li$ (bcc)	10 (48)	6 x 6 x 6	160
Mg_7Li	20 (256)	8 x 8 x 8	640
Mg_3Li ($L1_2$)	56 (864)	12 x 12 x 12	224
Mg_3Li (DO_{22})	30 (200)	10 x 10 x 4	240
Mg_3Li (DO_3)	20 (256)	8 x 8 x 8	320
MgLi ($L1_0$)	75 (500)	10 x 10 x 10	300
MgLi (B2)	56 (864)	12 x 12 x 12	112
MgLi (B32)	20 (256)	8 x 8 x 8	320
$MgLi_3$ ($L1_2$)	56 (864)	12 x 12 x 12	224
$MgLi_3$ (DO_{22})	30 (200)	10 x 10 x 4	240
$MgLi_3$ (DO_3)	20 (256)	8 x 8 x 8	320
$MgLi_7$	20 (256)	8 x 8 x 8	640
$MgLi_{15}$ (bcc)	10 (48)	6 x 6 x 6	160
Li (hcp)	96 (784)	14 x 14 x 8	192
Li (fcc)	56 (864)	12 x 12 x 12	224
Li (bcc)	56 (864)	12 x 12 x 12	112

Table 4.1: The number of k-points in the irrerucible part of the Brillouin zone used in the calculations for all stuctures considered. The numbers in brackets refer to the total number of k points sampled in the full Brillouin zone.

in the present calculations were set at 0.4 and 0.1 eV, respectively for alloys and 0.1 and 0.01 eV, respectively for elemental metals since their energy differences are very small.

4.4 Elasticity

The elastic properties of a solid are important because they relate to various fundamental solid-state properties, such as equation of state, phonon spectra, etc. [80]. From materials physics perspective, the elastic constants C_{ij} contain some of the more important information that can be obtained from ground-state total-energy calculations. Elastic constants for most pure metals are available over a wide range of temperature in the literature [81, 82]. In contrast, data for alloys and intermetallic compounds are much more limited. Although the bulk modulus is oftenhas been calculated, calculations of the other elastic constants are relatively scarce [83].

The elastic constants of a material describe its response to externally applied strain or, the stress required to maintain a given deformation. For small deformations we expect a quadratic dependence of the crystal energy E on the strain (Hooke's law). Both stress and strain have three tensile and three shear components, giving six components in total. The linear elastic constants form a 6x6 symmetric matrix, having 27 different components, such that $\sigma_i = C_{ij}\varepsilon_j$ for small stresses, σ, and strains, ε [82]. Any symmetry in the structure can make some of these components equal, and/or some strictly zero. A cubic crystal thus has only three different symme-

try elements (C_{11}, C_{12} and C_{44}) with each representing three equal elastic constants ($C_{11} = C_{22} = C_{33}$, $C_{12} = C_{23} = C_{31}$, $C_{44} = C_{55} = C_{66}$). A single strain with non-zero first and fourth components can give stresses relating to all three of these coefficients, yielding a very efficient method of obtaining elastic constants for the cubic system. A full account of the symmetry of stress, strain and elastic constants is given by Nye [84]. The elastic constants determine the response of the crystal to external forces, as characterized by bulk modulus (B), shear modulus (C'), Young's modulus (E), Poisson's ratio (ν) and shear anisotropy factor (A). They play an important part in determining the strength of the material. These elastic moduli are given by the following expressions for a cubic crystal:

$B = \frac{1}{3}(C_{11} + 2C_{12})$, $C' = \frac{1}{2}(C_{11} - C_{12})$, $\nu = \frac{C_{12}}{C_{11}+C_{12}}$ and $A = \frac{2C_{44}}{C_{11}-C_{12}}$.

The requirement of mechanical stability in a cubic crystal leads to the following restrictions on the elastic constants [85]:

$(C_{11} - C_{12}) > 0$, $C_{11} > 0$, $C_{44} > 0$, $(C_{11} + 2C_{12}) > 0$.

The single-crystal shear moduli for the {100} plane along the [010] direction and for the {110} plane along the [1$\bar{1}$0] direction in a cubic crystal are given by C_{44} and C', respectively. The shear constant C_{44} is related to an orthorhombic deformation, whereas the C' is related to a tetragonal deformation and its size reflects the degree of stability of the crystal with respect to a tetragonal shear [86].

For crystals with a tetragonal structure, such as $L1_0$ and DO_{22} , there are six independent elastic constants in the contracted matrix notation, C_{11}, C_{12}, C_{13}, C_{33},

C_{44}, and C_{66}. A set of six independent total-energy calculations is necessary to determine these elastic constants. The elastic moduli can be derived from these elastic constants as follows:

$B = \frac{1}{9}(2C_{11} + C_{33} + 4C_{13} + 2C_{12})$, $C' = \frac{1}{15}(2C_{11} + C_{33} - C_{12} - 2C_{13} + 6C_{44} + 3C_{66})$, $E = C_{33} - 2\nu C_{13}$, $\nu = \frac{C_{13}}{C_{11}+C_{12}}$ and $A_1 = \frac{2C_{66}}{C_{11}-C_{12}}$ (on basal plane), $A_2 = \frac{4C_{44}}{C_{11}+C_{33}-2C_{13}}$ (on (010) plane).

The requirement that the crystal be stable against any homogeneous elastic deformation places restrictions on the elastic constants, just as in the cubic case. For tetragonal crystals, these stability restrictions are as follows [85]:

$(C_{11}-C_{12}) > 0$, $(C_{11}+C_{33}-2C_{13}) > 0$, $C_{11} > 0$, $C_{33} > 0$, $C_{44} > 0$, $C_{66} > 0$, $(2C_{11} + C_{33} + 2C_{12} + 4C_{13}) > 0$.

A hexagonal crystal has 6 different symmetry elements ($C_{11}, C_{12}, C_{13}, C_{33}, C_{44,}$and C_{66}), only 5 of them are independent since $C_{66} = \frac{1}{2}(C_{11} - C_{12})$.

The stability restrictions do not tell us anything further about the relative magnitudes of the various elastic constants. The problem of ductile versus brittle response of crystals require their fracture strength in addition to their plastic deformability. Pugh [87] introduced the quotient of bulk modulus to shear modulus, B/C', for polycrystalline phases as a measure of fracture or toughness in metals. A high value of B/C' is associated with ductility and a low value with brittleness. The critical value which separates ductile and brittle materials is about 1.75 [80]. This parameter is mostly applied for cubic materials. The factor that measures the stability of a crystal

against shear is Poisson's ratio (ν). It provides more information about the characteristic of the bonding forces than any of the other elastic constants [88]. The smaller value of ν indicates that the compound is relatively stable against shear. It has been proved $\nu = 0.25$ is the lower limit for central-force solids and 0.5 is the upper limit, which corresponds to infinite elastic anisotropy [89].

In metals and alloys behaving like isotropic media, the Young's modulus is proportional to the bulk modulus when the Poisson's ratio is close to $\frac{1}{3}$. This is shown by the relation between hydrostatic bulk modulus and Young's modulus expressed by Poisson's ratio ν appearing in the relation $E = 3\,(1 - 2\nu)\,B$.

Chapter 5
RESULTS

5.1 Equilibrium Atomic Volume

In this chapter, the predicted cohesive properties are presented with discussions of various observed trends including the deviations from Vegard's law [108] displayed by the equilibrium atomic volumes and the variation in the heats of formation across the Mg-Li alloy series. This is then followed by a discussion of the electronic structure in the form of the density of states (DOS). The latter is used to provide a Jones-type analysis of the structural trends across the Li-Mg phase diagram as the average number of electrons per atom (e/a) changes from 1 to 2. Finally the elastic moduli are analysed and an interesting correlation with the relative energy difference between the corresponding fcc and bcc ordered superstructures is observed.

We performed geometry optimization calculations for all the Mg-Li systems illustrated in Figure 4.1 together with the end elements Mg and Li. We used the GGA-PBE exchange-correlation functional. We commenced the self consistent iterations using as an input the experimental lattice constants where available. We used a kinetic energy cut-off of $500\ eV$ with the number of **k**-points as specified in Table 4.1. These had been deduced from plots of the total energy against kinetic energy cut-off and total energy versus number of **k**-points, respectively, to optimize

our structures as discussed in section 4.3. Since our pseudopotential choice was ultrasoft, the CASTEP interface increased the recommended FFT grid automatically: this is required to reproduce accurately the augmentation charge [26]. Our calculated equilibrium lattice parameters and equilibrium atomic volumes are listed in Tables 5.1 and 5.2, for fcc- and bcc-based superstructures respectively, with some available experimental and theoretical results for comparison.

Figure 5.1 shows the predicted variation in equilibrium atomic volume across the Mg-Li alloy series. We see that with increasing Li composition the volume shrinks in a V-shaped manner with the minimum at the equiatomic composition for both the fcc- and bcc-based structures. This behaviour deviates from both Vegard's law [108] and Zen's law [115] , which assume a linear dependence on the lattice constant or mean atomic volume, respectively. This is illustrated for Zen's law in Fig. 5.1 by the solid and dashed lines. This trend is also observed in the earlier experiments of Levinson [106].

5.2 Equation of state and bulk modulus

The equation of state for metals is obtained by computing the pressure

$$P = -\frac{dE}{dV} \tag{5.1}$$

for different volumes V. The resulting P-V curves for these systems are shown in Figure 5.2. We observe from this plot that P increases as the volume is decreased

	Lattice constants (Å)				Volume (Å^3/atom)	
Structure	Calculated a_0	Experimental a	Calculated c_0	Experimental c	Calc. V_0	Exp. V
Hcp						
Mg	3.195	3.209[107]	5.211	5.211[107]	23.037	23.240[10
	3.195[109]		5.185[109]		22.912[109]	
Li	3.050	3.111[7]	4.922	5.093[7]	19.825	21.344[7]
	3.103[109]		5.068[109]		21.133[109]	
Fcc						
Mg	4.530				23.246	23.071[11
	4.524[109]				23.149[109]	
Mg_7Li	8.990				22.712	
Mg_3Li ($L1_2$)	4.458				22.154	
	4.478[110]				22.450[110]	
Mg_3Li (DO_{22})	4.481		8.724		21.895	
	4.453[110]		8.906[110]		22.073[110]	
MgLi ($L1_0$)	4.820		3.487		20.258	
	4.385[110]		4.385[110]		21.080[110]	
$MgLi_3$ ($L1_2$)	4.309				19.998	
	4.336[110]				20.374[110]	
$MgLi_3$ (DO_{22})	4.307		8.681		20.128	
	4.332[110]		8.664[110]		20.323	
$MgLi_7$	8.610	8.754[107]			19.942	20.964[10
Li	4.307	4.410[6]			19.973	21.442[6]
	4.386[109]				21.089[109]	

[6] Experiment at -196 $^\circ C$.
[107] Experiment at 20$^\circ C$.
[109] Calculated
[110] Calculated by exact muffin-tin orbitals (EMTO) method with GGA.

Table 5.1: Calculated hcp equilibrium lattice constants a_0 and c_0 for elementary Mg and Li and the calculated lattice constants a_0 for the underlying fcc lattices of ordered Mg-Li compounds. The calculated atomic volumes are also shown, together with available experimental and theoretical counterparts.

	Lattice constant (Å)		Atomic volume (Å^3/atom)	
Structure	Calculated a_0	Experimental a	Calculated V_0	Experimental V
Bcc				
Mg	3.585	3.573[107]	23.033	22.807[107]
	3.594[111]		23.238[111]	
$Mg_{15}Li$	7.136		22.714	
Mg_3Li (DO_3)	7.024		21.652	
	7.030[110]		21.713[110]	
MgLi (B1)	5.620		22.190	
MgLi (B2)	3.420	3.485[106]	19.996	21.163[106]
	3.434[110]	3.477[107]	20.25 [110]	21.018[107]
	3.380[112]		19.304[112]	
MgLi (B32)	6.948		20.964	
	6.676[112]		18.601[112]	
$MgLi_3$ (DO_3)	6.846		20.051	
	6.872[110]		20.280[110]	
$MgLi_3$ (bcc)		3.500[106]		21.437[106]
$MgLi_{15}$	6.842	7.010[113]	20.025	21.529[113]
	6.824[114]		19.861[114]	
Li	3.424	3.510[106]	20.068	21.622[106]
	3.478[109]	3.491[7]	21.044[109]	21.272[7]

[7] Experiment at 78 K.
[106] Experiment.
[107] Extrapolated hypothetical.
[107] Experiment at -183°C.
[112] Calculated using Linear combination-of-atomic-orbitals (LCAO).
[113] Experiment at 20°C.
[114] Calculated using LMTO.
[110] Calculated by exact muffin-tin orbitals (EMTO) method with GGA.

Table 5.2: The calculated bcc equilibrium lattice constants a_0 for elementary Mg and Li and the calculated lattice constants a_0 for the underlying bcc lattices of ordered Mg-Li compounds. The calculated atomic volumes are also shown, together with available experimental and theoretical counterparts

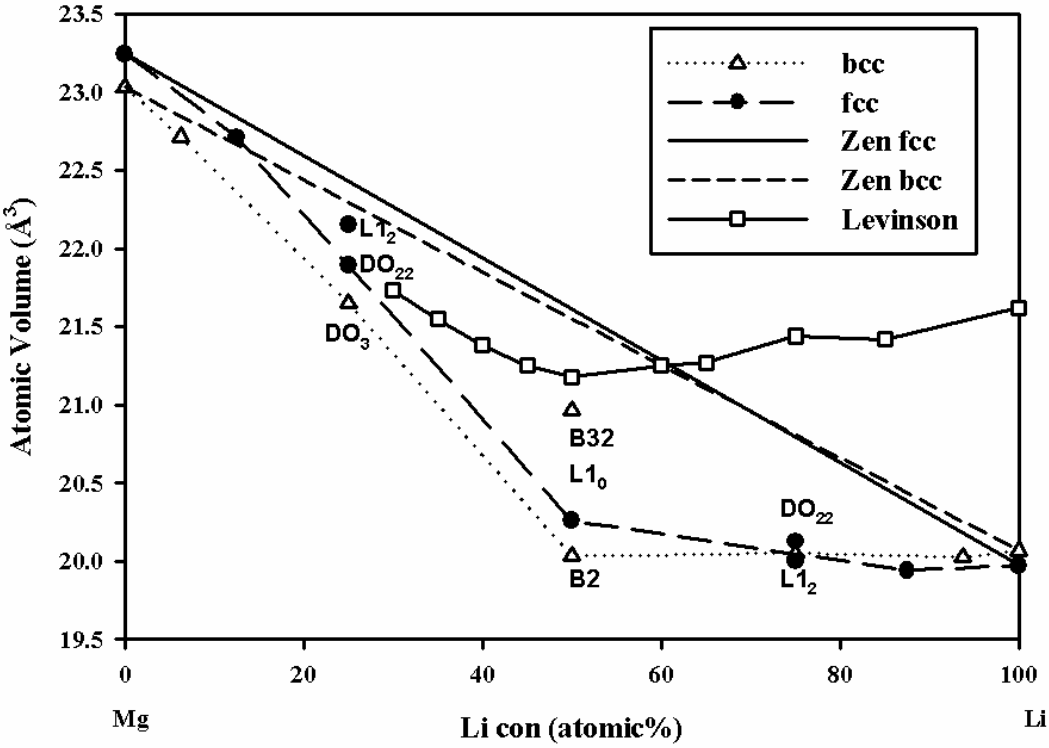

Figure 5.1: Atomic volumes of ordered Mg-Li compounds as a function of Li concentration (triangles and circles correspond, respectively, to bcc- and fcc-based superstructures) together with experimental data of Levinson [106]. Zen's law is indicated by solid lines with respect to both bcc- and fcc-based superstructures.

fcc-structure	Bulk Modulus (GPa)		
	Calculated		Experimental
	This work	Skriver [110]	
Mg	34.11		
Mg_7Li	33.99		
Mg_3Li ($L1_2$)	27.15	29.45	
Mg_3Li (DO_{22})	28.03	28.87	
MgLi ($L1_0$)	25.25	24.17	
Mg_3Li_7 (30 at.% Mg)			16.1[116]
$MgLi_3$ ($L1_2$)	19.07	18.76	
$MgLi_3$ (DO_{22})	17.49	18.84	
$MgLi_4$ (20 at.%Mg)	16.80		14.3[116]
$MgLi_7$	16.42		
$MgLi_9$ (10 at.%Mg)			13.2[116]
Li	13.92		

[110] Calculated by exact muffin-tin orbitals (EMTO) method with GGA.
[116] BCC phase at room temperature.

Table 5.3: The bulk moduli for fcc elemental Mg and Li as well as for fcc-based Mg-Li alloys

as expected. The equilibrium bulk modulus, which reflects the curvature of the binding energy curves or slope of the P-V curves at the equilibrium volume V_0, is defined by

$$B = -V_0 \left(\frac{dP}{dV} \right) = V_0 \frac{d^2E}{dV^2} \ . \tag{5.2}$$

The equilibrium bulk moduli for elemental Mg and Li in both fcc as well as bcc phases and for Mg-Li order structures with respect to the fcc and bcc lattices are given in Tables 5.3 and 5.4, respectively. We observe that the bulk moduli decrease monotonically with an increase in Li concentration. We see that our calculated bulk moduli agree reasonably well with other theoretical counterparts and fairly so with experiment.

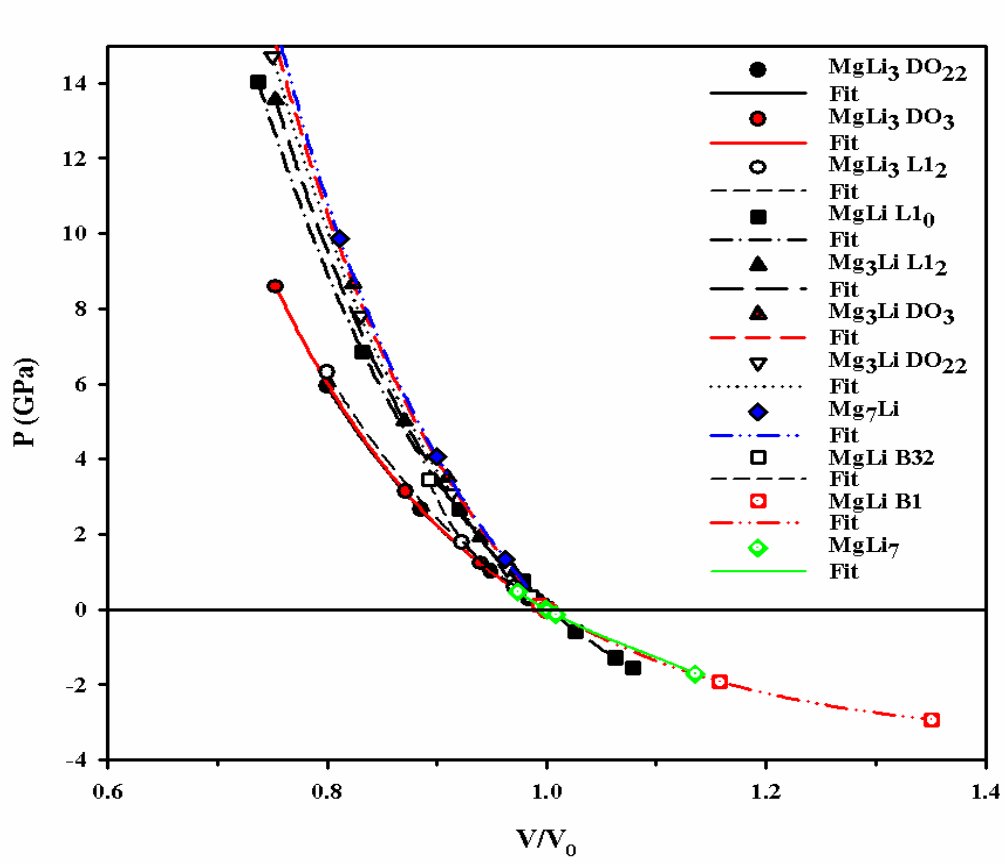

Figure 5.2: Equation of states for the bcc- and fcc-based Mg-Li alloys under study.

bcc-structure	Bulk Modulus (GPa)	
	Calculated	Experimental
Mg	37.57	
$Mg_{15}Li$	32.94	
Mg_3Li (DO_3)	32.76	
	30.47[110]	
65 at.% Mg		25.0[116]
MgLi (B1)	16.74	
MgLi (B2)	22.11	
	20.25[110]	
		20.7[116]
MgLi (B32)	25.25	
$MgLi_3$ (DO_3)	18.04	
	18.78[110]	15.0[116]
$MgLi_{15}$	23.12	
Li	12.00	12.6[144]

[110] Calculated by exact muffin-tin orbitals (EMTO) method with GGA.
[116] BCC phase at room temperature.

Table 5.4: The bulk moduli for bcc elemental Mg and Li as well as for bcc-based Mg-Li alloys

5.3 Heats of formation

The heat of formation is one of the prime thermodynamic ingredients in the free energy to determine phase diagrams, the other being entropy. Hence studying the relative stability of the different cubic-based superstructures, it is convenient to consider the formation energy (E_{form}) of each structure. The formation energy is responsible for the relative stability of the phases at low temperatures where entropic contributions are not important. The phase equilibria are determined by drawing the common tangent [117] lines between the free energy curves of neighbouring compounds. The heat of formation of the alloy $Mg_{1-x}Li_x$ is defined by

$$E_{form}^{Mg_{1-x}Li_x} = E_{total}^{Mg_{1-x}Li_x} - [xE_{solid}^{Li} + (1-x)E_{solid}^{Mg}] \tag{5.3}$$

where $E_{total}^{Mg_{1-x}Li_x}$ is the total energy of the alloy, E_{solid}^{Mg} and E_{solid}^{Li} are the total energies of the stable structures of elemental Mg and Li, and x and $(1-x)$ refer to the fractional concentrations of the constituent elements.

5.3.1 Li and Mg in hcp, fcc and bcc phases

The heats of formation (eq. 5.3) depend on finding the energies of the constituent elements in their ground state structure. As can be seen from Table 5.5, our results predict hcp Mg structure to be energetically favoured over the fcc and bcc structures, consistent with experimental and other theoretical results [118, 119, 120]. For elemental Li, the situation is more complicated. The stable structure of Li is bcc at

temperatures above $78°$K. Earlier work by Barrett [7] reported that at $78°$K the hcp phase coexists with the bcc phase, and that cold working at low temperatures produces the fcc phase at the expense of hcp and bcc phases, Li having undergone a martensitic transformation. However, a later study [8] showed that the ground-state structure of Li is neither hcp nor fcc, but a 9R-related complex close-packed structure suggested by Overhauser [9]. As shown in Table 5.5, our results found that hcp Li is more stable than both fcc and bcc at zero temperature, although we did not compute 9R due to the large size of its unit cell. However, there is only a very small energy difference between the phases, hcp being only $0.06\ meV$ more stable than fcc. Since it is well known that the phases of Li are extremely close in energy [5, 121, 122, 123, 124, 125, 126], geometry optimizations had to be performed with great caution. The smearing width is periodically halved during the planewave pseudopotential calculation. We used 0.01 and $0.1\ eV$ for minimum and maximum smearing widths respectively, since values as low as $0.01\ eV$ have been previously used to calculate the converged energy [25, 26]. However, we must stress that these energy differences are so small that even a change in choice of exchange-correlation functional can alter the predictions [121].

5.3.2 Fcc- and bcc-based ordered Mg-Li alloys

The calculated values of the heats of formation of the Mg-Li systems considered in this study are summarized in Table 5.6, with asterisks denoting the predicted most

Element	Phase	Equilibrium total energy E_0 (eV/atom)	Energy relative to hcp (meV/atom)	
			This work	Experiment [127]
Mg	hcp	-977.892621	0.00	0.000
	fcc	-977.877264	15.36	27.04
	bcc	-977.858844	33.78	32.27
Li	hcp	-190.029049	0.00	0.00
	fcc	-190.028985	0.06	0.48
	bcc	-190.027526	1.52	1.61

[127] Experimental thermodynamically based estimates using CALPHAD approach.

Table 5.5: Calculated equilibrium energies as well as energies relative to most stable phase, hcp, for pure elements (Mg and Li) in various phases. Experimental results are thermodynamic estimates within the CALPHAD approach.

stable phases amongst competing structures for a given stoichiometry. Figure 5.3 shows the plot of the heats of formation of the Mg-Li system versus composition. We see that the curve takes a V-shape, with its minimum at the equi-concentration MgLi compound. This is in agreement with the experimental heats of formation of liquid Mg-Li alloys at $1000°C$ [128] and the theoretical DFT results of Skriver [110]. This excellent agreement between theory and experiment is fortuitous, since the ordered structures should have heats of formation that are about 30% lower in energy than the corresponding enthalpies of formation of the disordered liquid state [129].

At 50-50 concentration, the B2 structure is clearly seen as the most stable phase, since it has the lowest formation energy amongst its competing counterparts (Table 5.6). Our calculations predict that the B2 structure is lower by 26 meV/atom than that of B32. These results agree quantitatively with the earlier pseudopotential calculations by Hafner and Weber [112], and Hafner [31], who found B2 to be lower in energy by $116\ meV/atom$ and $88\ meV/atom$ respectively. Our predicted heat of formation for the B2 structure of $-73.4\ meV/atom$ is in excellent agreement with Skriver's DFT result of $-73.5\ meV/atom$ [110]. Experimentally, a tendency towards B2 (CsCl) type ordering has been observed at low temperatures [106, 107]. Interestingly, the difference in the calculated energy difference of the $L1_0$ and B2 phases is small, which suggests that both phases might be present at very low temperatures, if only the kinetics were fast enough for phase transitions. We observed

Ordered structure	E_{form} (meV/atom)		
	This work	Skriver [110]	Experimental [128]
$A_{15}B$			
$Mg_{15}Li$ (bcc)	11.25		
A_7B			
Mg_7Li	-3.33		
A_3B			
Mg_3Li ($L1_2$)	-23.96	-21.2	
Mg_3Li (DO_{22})	-18.82	-20.7	
Mg_3Li (DO_3)	-38.32*	-48.7*	-39.2
AB			
MgLi (B2)	-73.41*	-73.5*	-56.7
MgLi (B32)	-47.72		
MgLi ($L1_0$) $c/a = 0.72$	-72.01		
$c/a = 1$	-44.16	-37.2	
AB_3			
$MgLi_3$ ($L1_2$)	-36.61	-28.3	
$MgLi_3$ (DO_{22})	-37.43*	-34.4	
$MgLi_3$ (DO_3)	-31.12	-37.4*	-31.0
AB_7			
$MgLi_7$	-20.00		
AB_{15}			
$MgLi_{15}$ (bcc)	-5.28		

[110] Calculated by exact muffin-tin orbitals (EMTO) method with GGA.
[128] Experiment for liquid alloys at 1000°C.

Table 5.6: Heats of formation of Mg-Li alloys predicted by this work and by Skriver [109] for ordered structures compared to experimental values for liquid alloys at 1000 degrees celsius [Mashovetz and Puchkov]. Asteriks denote the most stable phase at that composition predicted by this work and Skriver [109].

a huge energy difference between our $L1_0$ result and Skriver's. This was caused by the fact that Skriver did not relax the c/a ratio so that his underlying lattice is truly "fcc", hence MgLi ($L1_0$) becomes very unstable compared to B2, whilst ours was relaxed to $c/a = 0.72$. It became evident when we did a calculation with fixed ratio of $c/a = 1$ that our result and Skriver's were in reasonable agreement.

The heat of formation for Mg_3Li in the three phases (Table 5.6) shows clearly the preferred stability of the DO_3 phase over the $L1_2$ and DO_{22} phases. The heat of

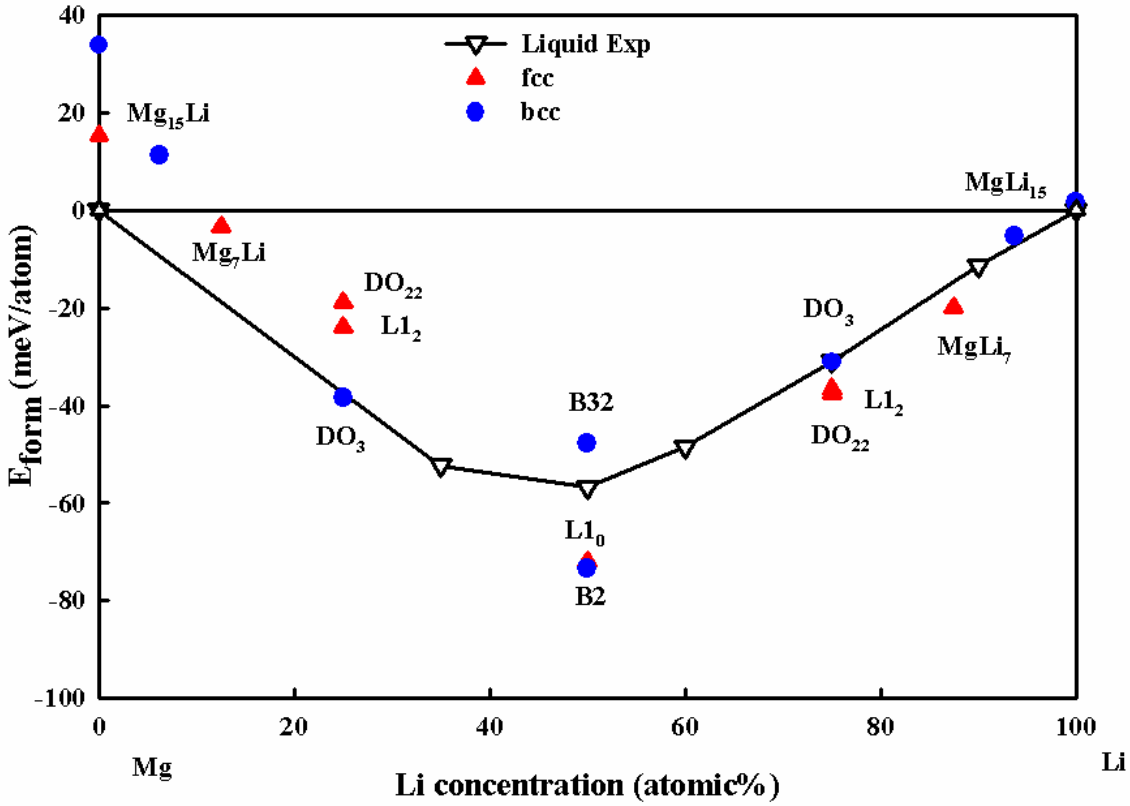

Figure 5.3: Predicted heats of formation for Mg-Li compounds compared with disordered experimental results[128] . The common tangent construction for stability limits of the different phases is indicated by the solid lines.

formation of Mg_3Li in the $L1_2$ structure is higher by $14.36\ meV/atom$ compared to the DO_3 phase, with the DO_{22} phase being even bigger. Our predicted phase stability ordering is the same as that of Skriver [110]. In the $MgLi_3$ compound, the DO_{22} structure has the lowest formation energy with the $L1_2$ and DO_3 phases lying only 0.82 and $6.32\ meV/atom$ higher, respectively. This slight difference between $L1_2$ and DO_{22} indicates a strong stability contest between these phases at this concentration. We see that Skriver predicts the DO_3 phase to be more stable than DO_{22}. However, this is probably because he did not relax the c/a axial ratio from its ideal value of 2.00. We found an equilibrium value of 2.02 (Table 5.1).

In Figure 5.3, the solid common tangent lines are constructed for the stability limits of the different phases. Among the structures considered, the most energetically favourable intermetallic phases at absolute zero are the DO_3 Mg_3Li, B2 MgLi, DO_{22} $MgLi_3$ and $MgLi_7$ compounds. The $L1_2$ and DO_{22} structures are metastable at 25% Li, while the B1, B32 and $L1_0$ structures are metastable at 50% Li. Our equilibrium calculations predict DO_3 to be the most stable structure at A_3B composition, while at AB_3 the DO_{22} structure shows more stability than its competitors.

The Mg-rich compounds, the bcc supercell $Mg_{15}Li$ and the fcc supercell Mg_7Li, lie well above the tangent line connecting hcp Mg (E_{form}= $0\ eV$) with DO_3 Mg_3Li. This clearly indicates the instability of the bcc and fcc Mg-Li compounds around this region. This instability supports Hafner's earlier work [31] that hcp Mg-Li compounds are dominant in the region with less than 18% Li concentration. The for-

mation energy of Mg_3Li in both the DO_{22} and $L1_2$ structures lie above tangent line, which indicates the instability of the fcc lattice in this region. The energetically favoured phase is DO_3. Most of Mg-Li compounds at the Li-rich side lie either exactly or very close to the line connecting B2 MgLi with elemental hcp Li. As far as the stability is concerned in this region, fcc-based compounds are having an upper hand over the bcc-based compounds. In both regions, our predicted stability profile is in full agreement with Hafner's earlier work [31] on disordered Li-Mg solid solutions using second order perturbation theory.

5.4 Electronic density of states

Mg and Li are very good nearly-free-electron metals. This implies that their electronic properties can be understood by first considering those of a free electron gas, in which the eigenvalues E vary parabolically with the wave vector $\mathbf{k}$ as $E = (\hbar^2/2m)\mathbf{k}^2$. Filling up these states with 2 electrons each following Pauli's exclusion principle, we arrive at the concept of the Fermi surface, which is spherical for a free electron gas. As is well known, the corresponding density of states $n(E)$ of a free electron gas varies as the square root of the energy.

The electronic densities of states (DOS) for the hcp, fcc and bcc phases of Mg and Li are presented in Figure 5.4, using the CASTEP plane-wave methodology as discussed in section 3.6. We have taken the Fermi level E_F as the zero energy. The occupied part of the DOS for both Mg and Li in all three lattices show approximate

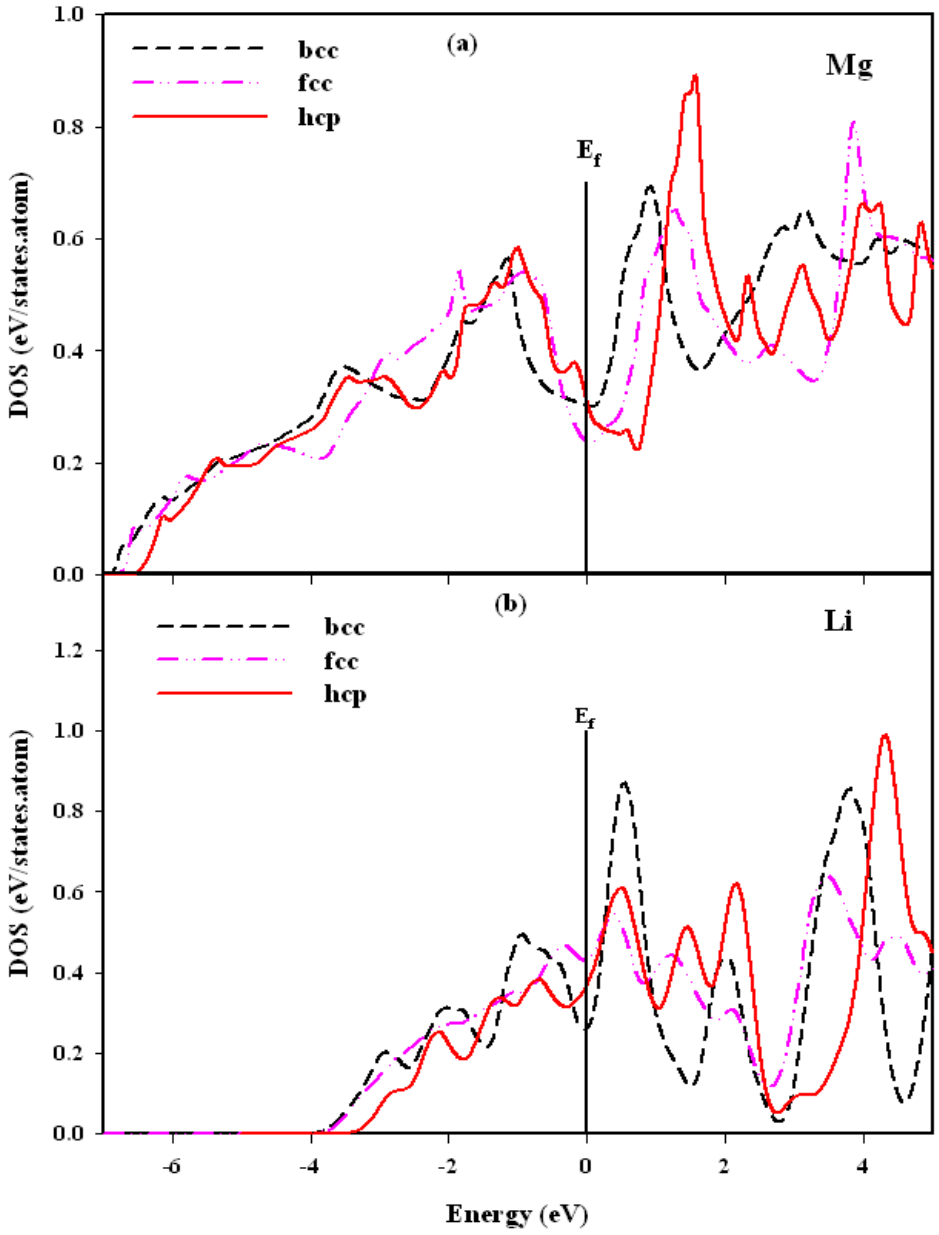

Figure 5.4: Density of states from CASTEP for elemental (a) Mg and (b) Li atoms in hcp, fcc and bcc lattices.

free-electron behaviour. This confirms that Mg and Li are good nearly-free electron (NFE) metals since their occupied DOS are only a relatively small perturbation of the free-electron density of states. However, we observe that Li, in all its three considered phases, displays very strong deviations from free-electron behaviour above the Fermi energy. This is a direct consequence of this first-row element having no p core electrons. This leads to large energy gaps opening up at the Brillouin zone boundary, and hence large deviations from free-electron behaviour in the unoccupied region of the DOS above E_F.

The partial and total DOS for the Mg-Li ordered structures with respect to fcc- and bcc-based lattices are shown in Figures 5.5-5.9. They agree with other DFT calculations in the literature [111, 114, 133]. We see that for all these different ordered phases the occupied region of the total DOS is approximately free-electron like. The partial DOS reflects the primarily s-type bonding on the Li sites, but the hybridized s-p bonding at the Mg sites, as expected for these monovalent and divalent metals, respectively. Table 5.7 gives the calculated DOS at the Fermi level, $n(E_F)$, for the 1:1 and 3:1 stoichiometries.

This relation between structural stability and the behaviour of the DOS in the vicinity of the Fermi energy can be formalized by a Jones-type analysis [134]. Using a rigid-band model, the theory shows how structure in the density of states translates into an energy difference for competing phases as a function of the electron count. Within the rigid-band approximation we assume that the bands of hcp, fcc, and bcc

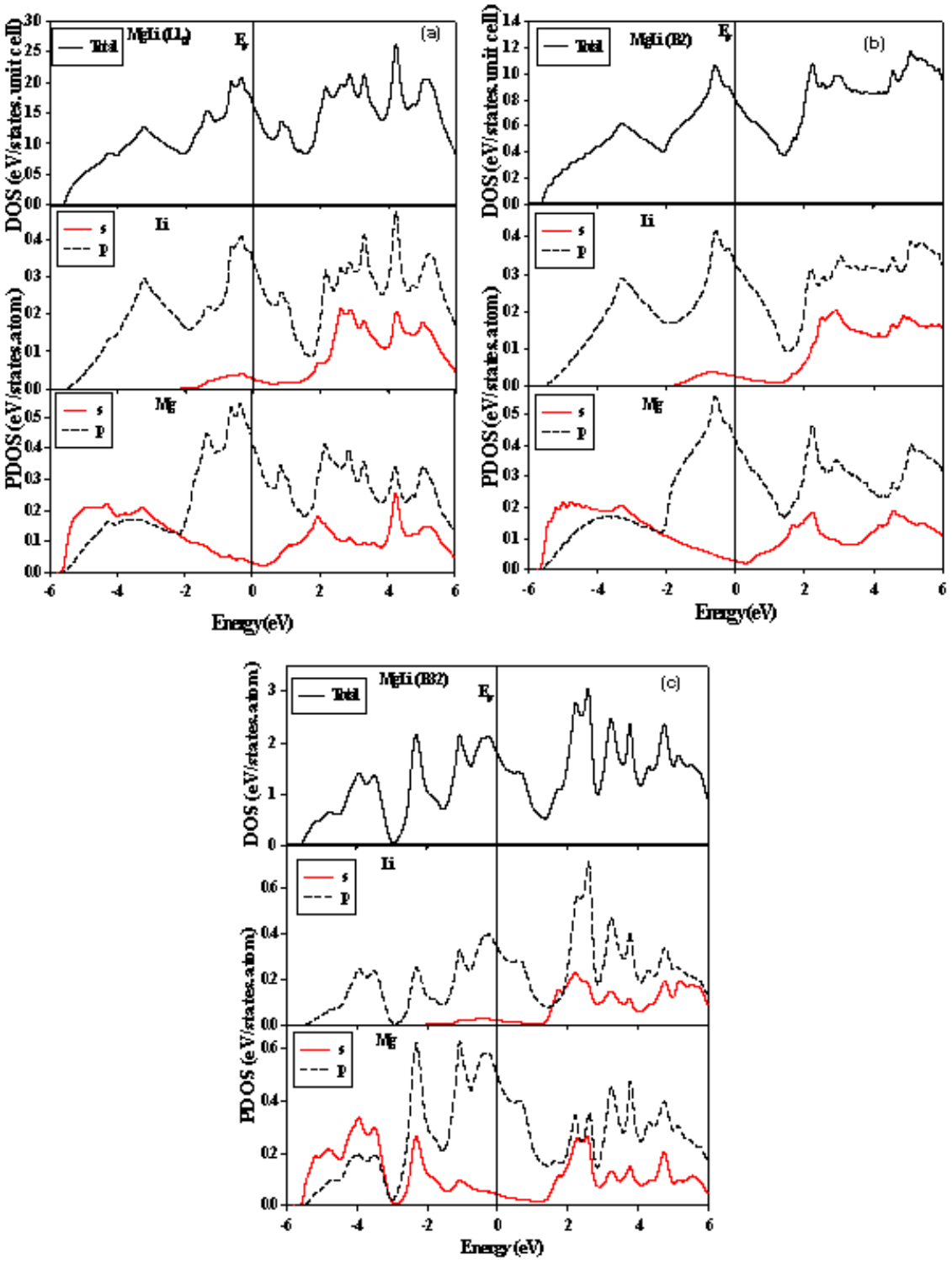

Figure 5.5: The total density of states (DOS) and partial density of states (PDOS) for MgLi compound in (a) $L1_0$, (b) B2 and (c) B32 structures, respectively.

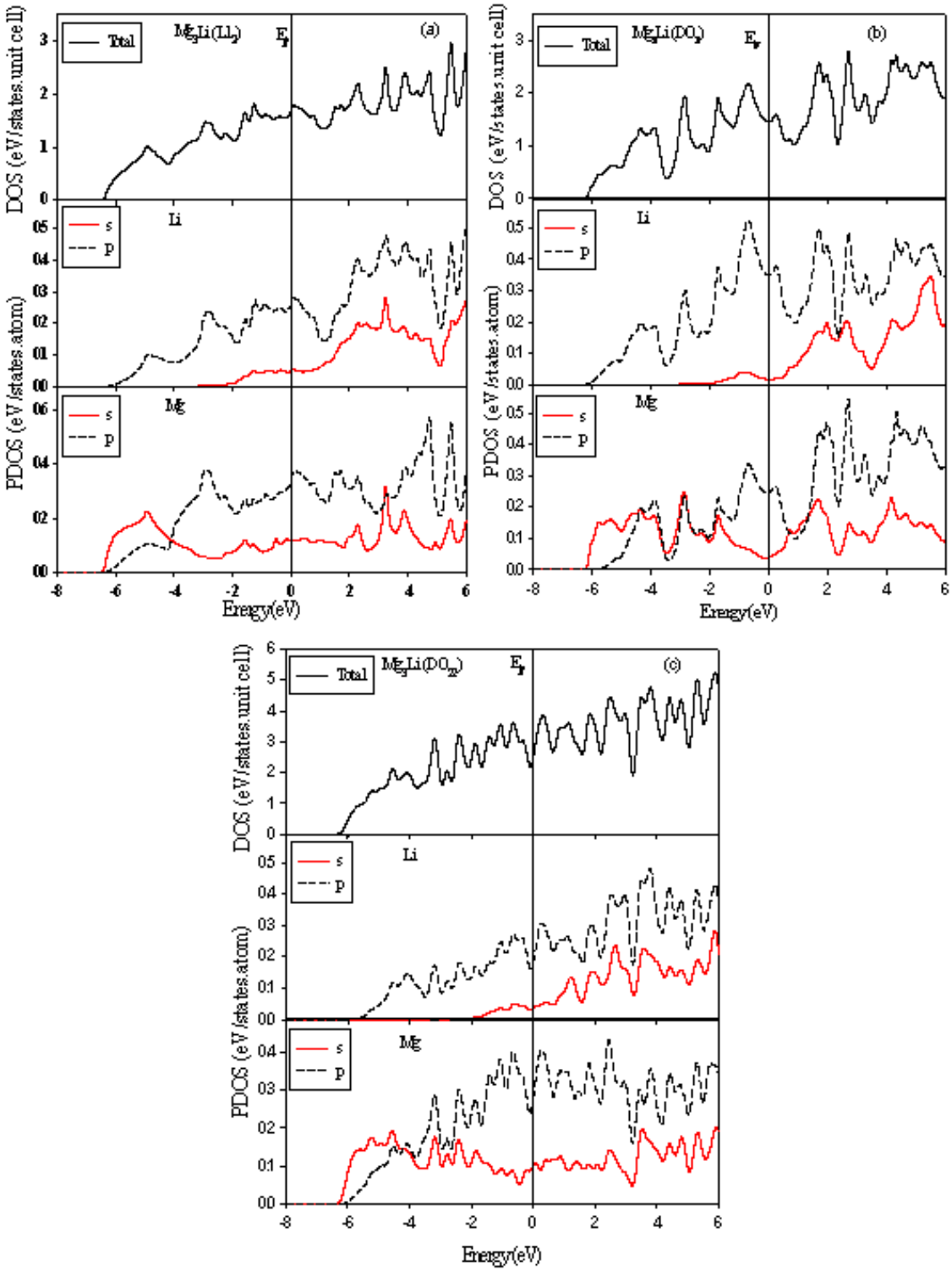

Figure 5.6: Total and partial density of states for Mg_3Li composition in (a) $L1_2$, (b) DO_3 and (c) DO_{22} structures.

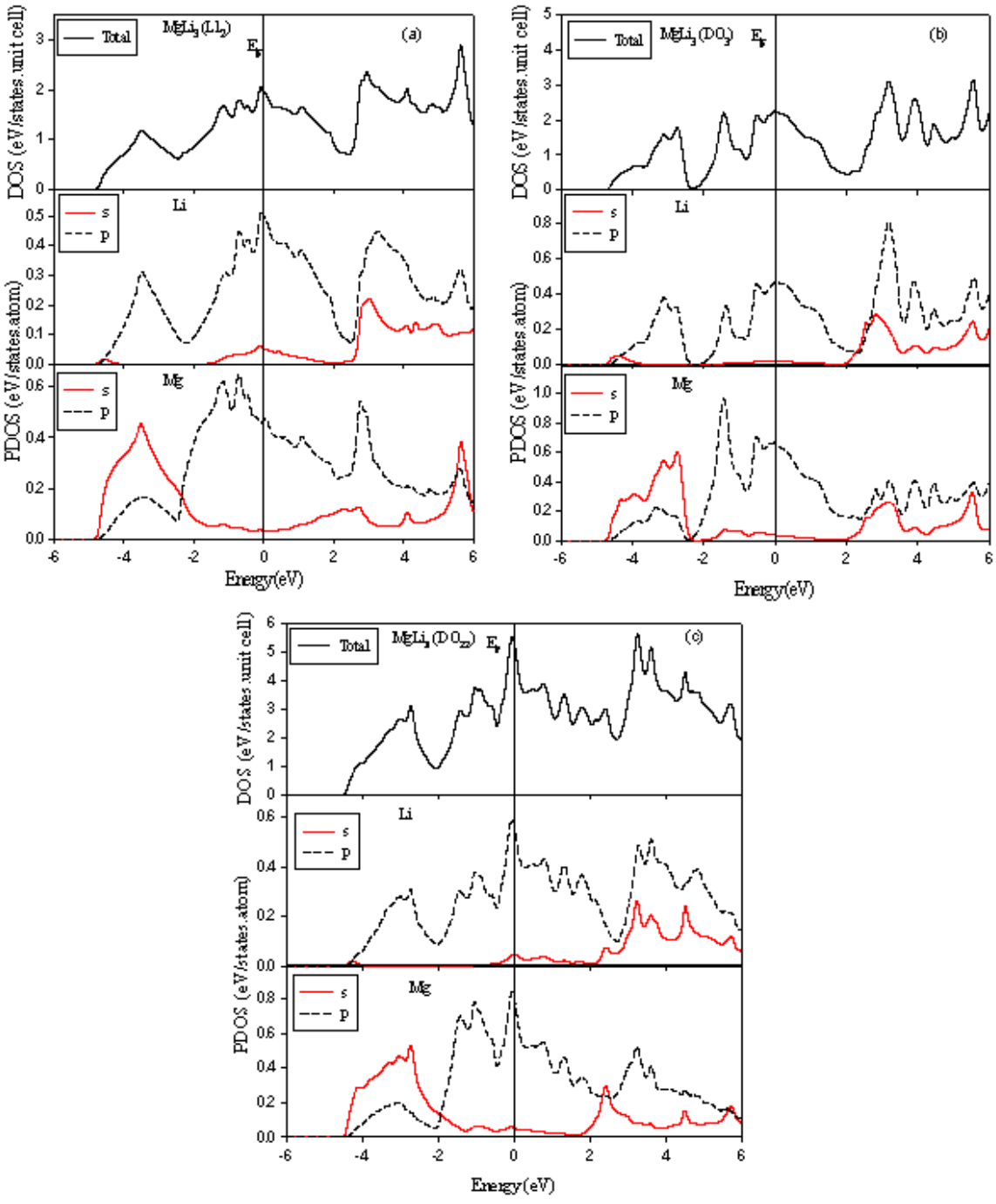

Figure 5.7: Total and partial density of states for $MgLi_3$ composition in (a) $L1_2$, (b) DO_3 and (c) DO_{22} structures.

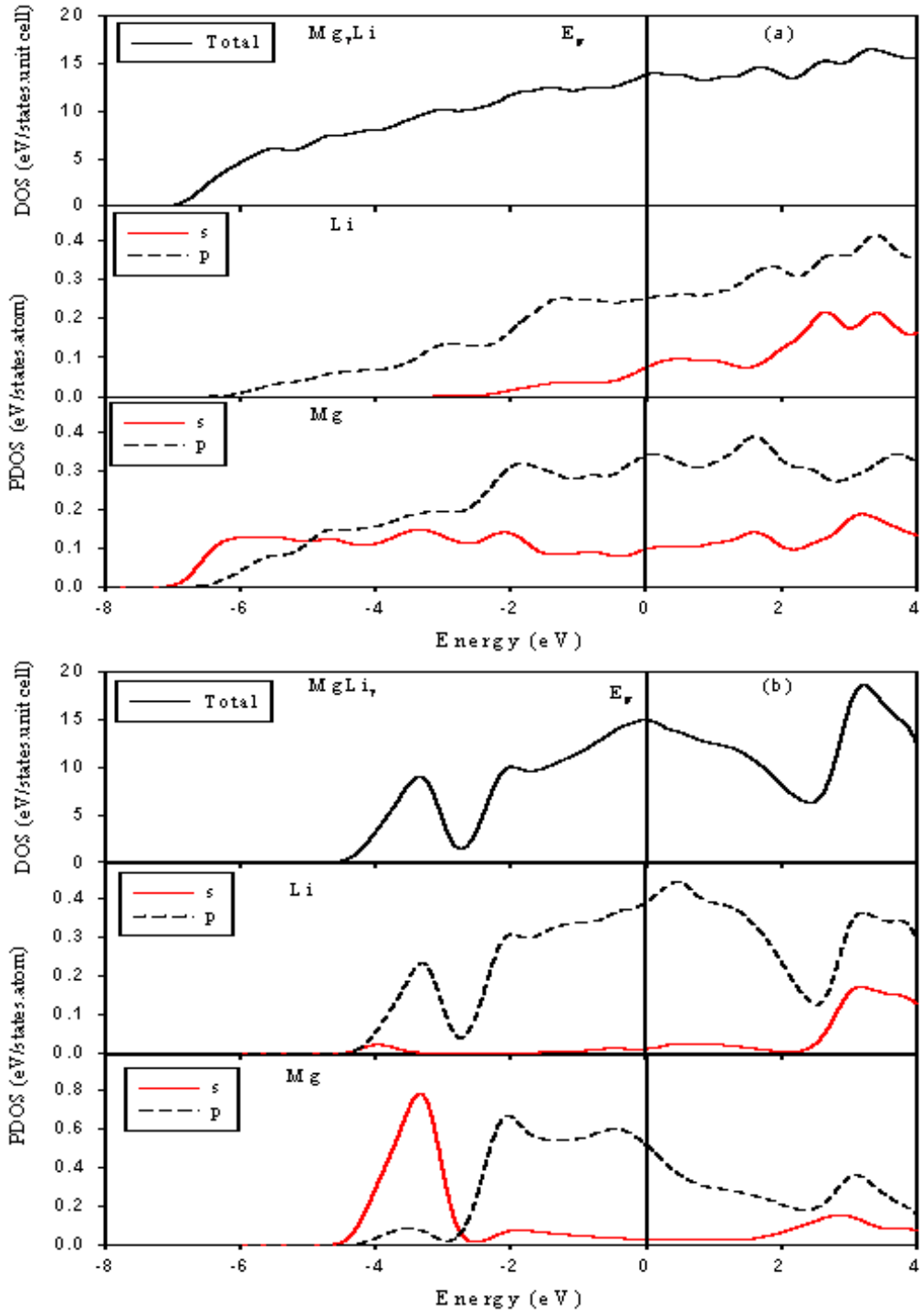

Figure 5.8: The total density of states (DOS) and partial density of states (PDOS) of fcc-based superstructures, (a) Mg_7Li and (b) $MgLi_7$, respectively.

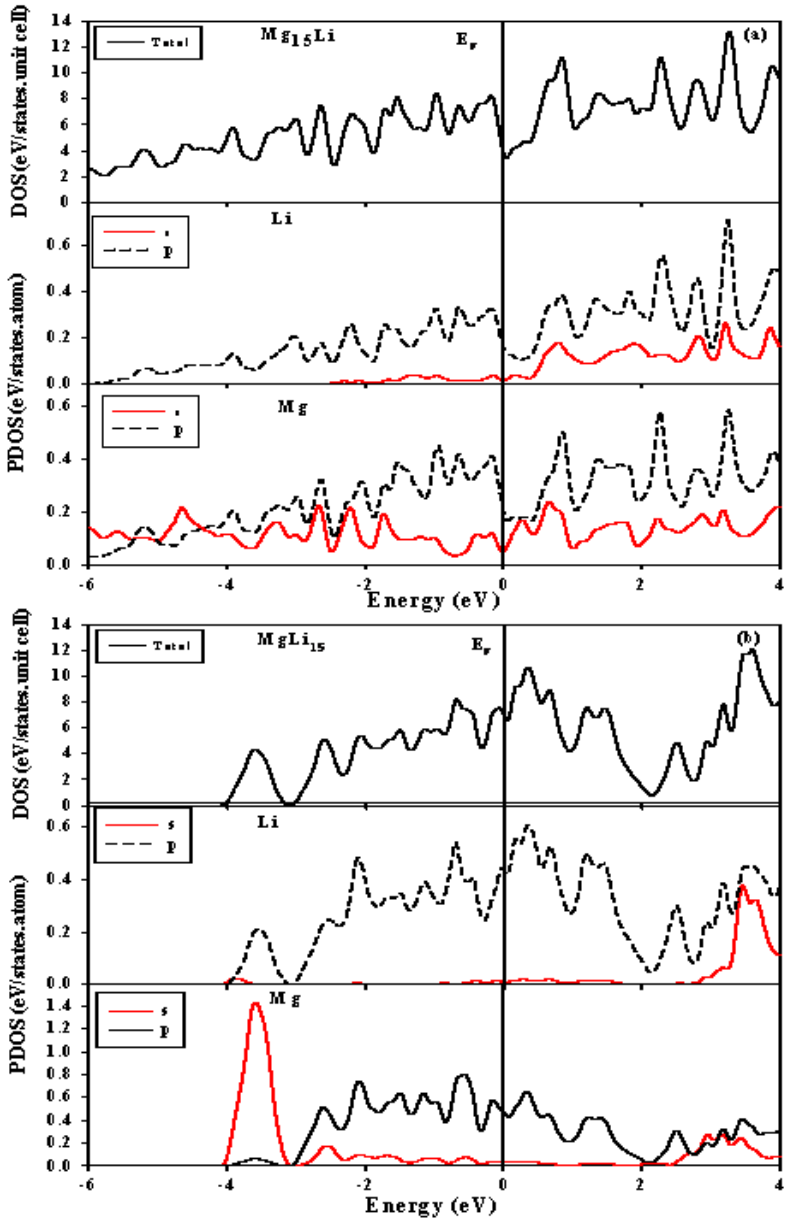

Figure 5.9: The total density of states (DOS) and partial density of states (PDOS) of bcc-based superstructures, (a) $Mg_{15}Li$ and (b) $MgLi_{15}$, respectively.

Compound	Structure	$n(E_F)$ (states/eV/atom)
Mg_3Li	$L1_2$	0.417
	DO_{22}	0.312*
	DO_3	0.367
MgLi	B2	0.399*
	B32	0.445
	$L1_0$	0.412
$MgLi_3$	$L1_2$	0.346*
	DO_{22}	0.669
	DO_3	0.564

Table 5.7: The total density of states at E_F, n(E_F) (in states/eV per atom), of Mg_3Li and $MgLi_3$, in $L1_2$, DO_{22} and DO_3 phases, and MgLi in B2, B32 and $L1_0$ phases, respectively. Asteriks denote the predicted stable phase.

lithium remain unchanged (or rigid) on alloying. A Jones analysis then states that the structural energy difference between any two lattices at the same atomic volume is given by

$$\Delta U = \Delta U_{band} = \Delta \left[\int^{E_F} E n(E) dE \right], \tag{5.4}$$

where $n(E)$ is the electronic density of states (DOS) per atom. The Fermi energy E_F is determined by the number of valence electrons per atom, $N \equiv e/a$, according to

$$N = \int^{E_F} n(E) dE. \tag{5.5}$$

Jones showed that the energy difference equation (5.4) allows us to link the relative stability of competing structures to the relative behaviour of the corresponding DOS. To help us understand the behaviour of the bandstructure energy, ΔU_{band}, we exploit the following expressions for the first and second derivatives of ΔU_{band} (equation 5.4) with respect to the electron number, N, as follows:

$$\frac{d}{dN}(\Delta U_{band}) = \Delta \left[\frac{dE_F}{dN} E_F n(E_F) \right] = \Delta E_F, \tag{5.6}$$

$$\frac{d^2}{dN^2}(\Delta U_{band}) = \Delta \left[\frac{1}{n(E_F)} \right], \tag{5.7}$$

where $n(E_F)$ is the DOS at the Fermi energy for the electron number $N = e/a$. Taking the difference of equation (5.6) for two different structures, we see that the

derivative of the energy difference is zero at certain special band fillings for which the two Fermi energies are equal. At these values of N, the bandstructure energy differance ΔU_{band} is extremal or possibly (in rare cases) a saddlepoint. To identify a maximum or a minimum, we take the difference of the inverses of their DOS at E_F, as given on the right-hand side of equation (5.7). If one of the structures has a lower DOS at this Fermi level, an extremum is present and this structure has a lower energy.

We employed the ab initio TB-LMTO-ASA (tight-binding-linear muffin-tin orbitals within atomic sphere approximation) method [39, 135, 136] to calculate the DOS for the hcp, fcc and bcc Li structures using the equilibrium cell parameters predicted by the CASTEP code (Section 4.4). To simulate the alloying with Mg, we keep the Li band structures for hcp, fcc and bcc structures fixed and calculate the bandstructure energies for an electron number varying between 0 and 2.

The difference of the bandstructure energies as a function of electron number is shown in Figure 5.10, together with the Fermi energy difference and DOS, all plotted against $N = e/a$ rather than energy. The top panel is the output quantity we are interested in, namely the bandstructure energy difference. The hcp-fcc energy difference curve has a minimum around $N = 1.0$ where the hcp DOS is lowest and a maximum around $N = 1.6$ where the fcc DOS is lowest, whereas the hcp-bcc curve has a minimum around $N = 1.1$ where the hcp DOS is lowest and a maximum around $N = 1.75$ where the bcc DOS is lowest. The middle panel shows

the first derivative of the energy function, i.e. the Fermi energy difference ΔE_F. This quantity has a positive slope where the hcp DOS lies below both the fcc and bcc DOS, and vice versa. The bottom panel presents the input, namely the DOS functions for the different phases. The central point is that this gives essentially the second derivative of ΔU_{band}. Thus, where the bcc DOS lies above the fcc DOS, the curvature of the energy difference function is such that the bcc structure will eventually become more stable. We see that with increasing electron concentration, the sequence of stable phases is hcp-fcc-bcc-hcp, in agreement with previous theoretical predictions [31].

5.5 Elastic properties

From the perspective of materials physics, the elastic constants C_{ij} contain some of the more important information that can be obtained from ground-state total-energy calculations. A given crystal structure cannot exist in a stable or metastable phase unless its elastic constants obey certain relationships. The C_{ij} also determines the response of the crystal to external forces, as characterized by the bulk modulus, shear modulus, Young's modulus, and Poisson's ratio, and so play an important role in determining the strength of a material [81]. First-principles calculations that use periodic boundary conditions assume the existence of a single crystal, so all elastic constants can be determined by direct computation. The calculated C_{ij} can then be used to check the experimental bulk and shear moduli, if available, and to calibrate

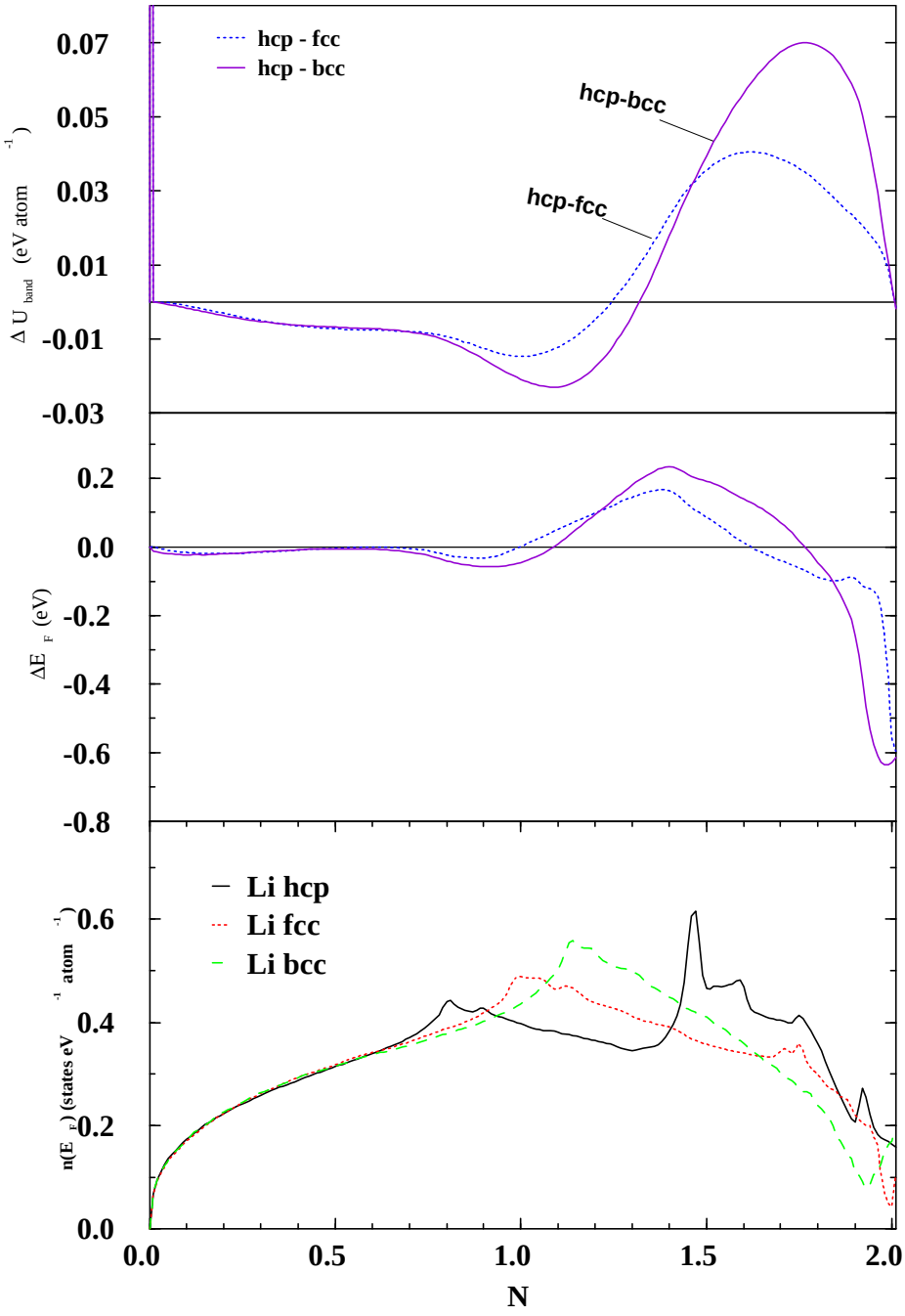

Figure 5.10: Energy difference, the Fermi energy difference and density of states plotted against electron concentration. The plot begins at $N = 0$ so Li occurs in the middle of the diagram where $N = 1$ whilst Mg occurs where $N = 2$.

model calculations. In addition, the elastic constants can be used to check the phase stability of proposed compounds [137, 138]. First-principles calculations can thus be used to predict the existence and properties of new materials and phases. In a theoretical search for new materials, an interesting and important area of research is to study binary compounds that exhibit high melting temperatures and large elastic constants (which roughly correlate with "strength"). These alloys might be good candidates for new structural materials, were they are not brittle [81]. For a cubic crystal to be mechanically stable it has to satisfy the following criterion: $B = (C_{11} + 2C_{12})/3 > 0$, $C' = (C_{11} - C_{12})/2 > 0$, $C_{44} > 0$ at the equilibrium of the equation of state, where B and C' are the bulk and shear modulus, respectively.

We performed calculations of the elastic moduli of Mg-Li alloys using CASTEP in Materials Studio version 3.0 [96]. Practical methods of determining the elastic coefficients from first principles usually set either the stress (or the strain) to a small finite value, optimize any free parameters of the structure, and calculate the strain (or stress). With a careful choice of the applied deformation, the elastic moduli can then be determined. Applying a given homogeneous deformation (the strain) and calculating the resulting stress requires far less computational effort, since the unit cell is fixed and only the ionic positions require optimization. This is the method implemented in the current work. The elastic properties were calculated by computing the components of the stress tensor for small strains using the method developed by Nielsen and Martin [139]. For small strain, the $C_{11}$and C_{12} elastic constants are

derived from the harmonic relation $C_{11} = \sigma_1/\epsilon_1$ and $C_{12} = \sigma_2/\epsilon_1$, where σ_i and ϵ_i represent respectively, the stress and the applied strain. The macroscopic stress in the solid is computed for a small strain by the use of the stress theorem, and the forces on the atoms are derived from the Hellman-Feynman theorem [102]. For an ϵ_4 strain (uniaxial strain in the (111) direction) there are internal displacements of the sublattices, and the atomic positions in the unit cell are not determined only by symmetry. Kleinmann [140] defines an internal strain parameter ξ that describes the displacements of the atoms.

The application of strain on the lattice implies a lowering of symmetry from that of the crystal, therefore very accurate total-energy calculations are required since the energy differences involved are of the order of 10 to 1000 $\mu eV/atom$. This circumstance requires the use of a fine **k**-point mesh. The calculations were considered converged when the maximum force on atoms was below 0.01 $eV/\mathring{A}$, the total energy change per atom was less than $4\text{x}10^{-4}$ $eV/atom$ and the displacement of atoms was below $4\text{x}10^{-4}\mathring{A}$. Both the energy and the stress were Pulay corrected to reduce any remaining finite basis set errors. The calculations were done at our theoretically determined (equilibrium) lattice constants for each structure, with a plane-wave basis set defined by an energy cut-off of 500 eV for pure elements and 400 eV for the ordered superstructures, a very small smearing width of 0.1 eV and sufficient sets of **k**-points. These parameters are essential because the Fermi energy and hence the total energy depend quite sensitively on them.

For each of the structures, six different values of the strain ± 0.0008, ± 0.0024 and ± 0.004 were used. The value of the stress is calculated for each strain. A linear fit of the stress-strain relationship for each component of the stress is computed and its gradient provides the value of the elastic constant. With our choice of special **k**-points in the full Brillouin zone and cut-off energy, the energy per atom was converged to $0.1\ meV/atom$ and $4\ meV/atom$ or less for pure elements and superstructures, respectively.

The calculated elastic constants for the Mg-Li systems are compared to available experimental data and the results of other calculations in Table 5.8. We find that the elastic constants of pure Mg in the hcp phase are in acceptable agreement with experimental results [130] as well as previous theoretical results [141] with the exception of C_{44} which is about 50% too small. The elastic constants of the fcc lattice Mg are also in good agreement with the available theoretical results while the bcc phase is found to be mechanically unstable, since the tetragonal shear modulus C' is negative. Our results for pure Li show mechanical stability in all three phases with the elastic constants being in good agreement with both experimental [143] and previous theoretical results [81, 141], except for the case of C_{11} and C_{44} of the bcc lattice which are overestimated.

Our calculated elastic constants for tetragonal systems show a small value of C_{44} in comparison to $C_{66,}$ which means that the tetragonal unit cell is more easily deformed by a pure shear about **a** and **b** axes in comparison to the **c** axis, with the

Composition	Structure	C_{11} GPa	C_{12} GPa	C_{44} GPa	C_{13} GPa	C_{33} GPa	C_{66} GPa	B GPa	$V_0\frac{d^2E}{dV^2}$ GPa
Mg This work	hcp	59.84	24.25	8.31	16.09	70.56	17.80	33.67	
Calculated[141]	hcp	66.20	22.10	18.00	16.60	62.50	22.05	33.94	
Experiment[130]	hcp	63.48	25.94	18.42	21.70	66.45	18.77	35.40	
Mg This work	fcc	42.75	30.96	23.09	-	-	-	34.89	34.11
Calculation[142]	fcc	46.00	27.40	30.00	-	-	-	33.60	
Mg This work	bcc	25.65	39.41	35.96	-	-	-	34.82	37.57
$Mg_{15}Li$ This work	bcc	55.77	24.70	50.93	-	-	-	35.06	32.94
Mg_7Li This work	fcc	22.21	29.47	24.23	-	-	-	27.05	33.99
Mg_3Li This work	$L1_2$	25.78	29.93	24.50	-	-	-	28.54	27.15
Calculated[110]									29.45
	DO_{22}	24.30	28.17	30.44	27.64	23.63	31.13	26.60	28.03
Calculated[110]									28.87
	DO_3	39.96	25.59	41.03	-	-	-	30.38	32.76
Calculated[110]									30.47
MgLi	B2	37.51	19.70	25.91	-	-	-	25.64	22.11
Calculated[110]									20.25
Exp.[128] 55% Mg	B2	32.20	19.80	26.60	-	-	-	23.90	
Exp.[128] 45% Mg	B2	28.50	20.50	19.40	-	-	-	23.20	
	B32	30.99	24.55	28.55	-	-	-	26.70	25.25
	$L1_0$	53.66	1.37	33.57	19.95	31.18	10.98	24.47	25.25
Calculated[110]									24.17
$MgLi_3$ This work	$L1_2$	25.76	15.94	18.68	-	-	-	19.21	19.07
Calculated[110]									18.76
	DO_{22}	28.86	13.86	21.66	14.49	27.37	23.27	18.97	17.49
Calculated[110]									18.84
	DO_3	19.42	17.79	15.42	-	-	-	18.33	18.04
Calculated[110]									18.78
$MgLi_7$ This work	fcc	15.83	16.95	11.70			-	16.58	16.42
$MgLi_{15}$ This work	bcc	18.24	13.25	11.52	-	-	-	14.92	23.12
Li This work	hcp	24.34	4.76	6.37	4.54	24.86	9.79	11.25	
Li This work	fcc	17.51	11.42	9.31	-	-	-	13.45	13.92
Calculated[81]	fcc	14.10	7.80	8.60	-	-	-	9.90	
Li This work	bcc	19.65	10.93	16.12	-	-	-	13.84	12.00
Calculated[141]	bcc	13.00	11.00	11.40	-	-	-	11.60	
Calculated[81]	bcc	15.60	14.80	11.20	-	-	-	10.60	
Experiment[143]	bcc	14.50	12.10	11.60	-	-	-	13.00	
Experiment[144]	bcc	13.50	11.40	8.80	-	-	-	12.10	

Table 5.8: Calculated elastic properties of Mg-Li alloys at equilibrium lattice parameters. The bulk moduli determined from elastic constants is compared with the ones calculated from equation of states.

Composition	Structure	C' GPa	B/C'	E GPa	ν	A
Mg This work	hcp	15.80	2.13	64.41	0.19	$A_1 = 1.00$
						$A_2 = 0.34$
Calculated[141]	hcp	20.92	1.62	56.26	0.19	-
Experiment[130]	hcp	-	-	45.00	0.35	-
Mg This work	fcc	5.89	5.92	16.75	0.42	3.92
Calculation[142]	fcc	9.30	3.61	25.54	0.37	3.23
Mg This work	bcc	-6.88	5.06	-22.09	0.61	-5.23
$Mg_{15}Li$ This work	bcc	15.54	2.26	40.60	0.31	3.28
Mg_7Li This work	fcc	-3.63	7.45	-11.41	0.57	-6.28
Mg_3Li This work	$L1_2$	-2.08	13.72	-6.38	0.54	-11.81
	DO_{22}	17.65	1.51	-5.50	0.53	$A_1 = -16.09$
						$A_2 = -16.57$
	DO_3	7.19	4.23	19.97	0.39	5.71
MgLi This work	B2	8.91	2.88	23.94	0.34	2.91
Experiment[128] 55% Mg	B2	8.33	-	17.12	0.38	4.29
Experiment[128] 45% Mg	B2	5.44	-	11.35	0.42	4.85
	B32	3.22	8.29	9.30	0.44	8.87
	$L1_0$	22.11	1.11	16.71	0.36	$A_1 = 0.42$
						$A_2 = 2.99$
$MgLi_3$ This work	$L1_2$	4.91	3.91	13.58	0.38	3.80
	DO_{22}	16.13	1.18	17.54	0.34	$A_1 = 3.10$
						$A_2 = 3.18$
	DO_3	0.82	22.35	2.42	0.48	18.92
$MgLi_7$ This work	fcc	-0.56	29.60	-1.70	0.52	-20.89
$MgLi_{15}$ This work	bcc	2.50	5.97	7.09	0.42	4.62
Li This work	hcp	2.32	4.85	23.44	0.16	$A_1 = 1.00$
						$A_2 = 0.63$
Li This work	fcc	3.05	4.42	8.49	0.39	3.06
Calculated[81]	fcc	5.80	1.71	14.00	0.35	2.73
Li This work	bcc	4.36	3.17	11.83	0.36	3.70
Calculated[141]	bcc	1.00	11.60	2.91	0.46	11.40
Calculated[81]	bcc	3.40	3.12	9.30	0.40	16.70
Experiment[144]	bcc	3.90	3.10	10.50	0.36	8.38

Table 5.9: Other derived elastic moduli of Mg-Li alloys, namely shear modulus (C'), the ratio of bulk modulus to shear modulus (B/C'), Young's modulus (E), Poisson's ratio (v) and the shear anisotropy factor (A).

exception of $L1_0$ structure wherein the opposite is the case. The small C_{44} value indicates that Mg-Li alloys are marginally stable with respect to the $\langle 010 \rangle$ shear on the (010) plane in this region.

In Table 5.9, we list the values of B/C' of Mg-Li alloys together with their shear modulus (C'), Young's modulus (E), Poisson's ratio (ν) and shear anisotropy factor (A). The bulk moduli decrease monotonically with the addition of Li content. The bulk moduli obtained from elastic constants agrees well with the experimental and other previous theoretical results including the ones extracted from equation of states. The B/C' values of 1.11, 1.18 and 1.51 for MgLi ($L1_0$), $MgLi_3$ (DO_{22}) and Mg_3Li (DO_{22}) , respectively, suggest that these compounds to be brittle, while the remaining ones appear to be ductile since their values are above the critical value of 1.75. The values of B/C' for all our Mg-Li systems, except for compounds listed above, are generally larger than those of pure elements, Mg and Li. It is also interesting to note that cubic Mg_3Li (DO_3) structure is the only phase that is stable at this concentration and has a positive value of Young's modulus E. For most of our structures, the derived ν is slightly higher than the isotropic value of $\frac{1}{3}$, thus resulting to E being less than B. We also observed that an increase in Li content increases the Poisson ratio as well as the anisotropy.

The elastic constants of our cubic Mg-Li systems listed in Table 5.8 obey the stability conditions as outlined in Section 4.4, including the fact that C_{12} must be smaller than C_{11}, except for Mg bcc, Mg_7Li, Mg_3Li ($L1_2$) and $MgLi_7$ structures. The

conditions also lead to a restriction on the magnitude of B. Since B is a weighed average of C_{11} and C_{12} and stability requires that C_{12} be smaller than C_{11}, we are then left with the result that B is required to be intermediate in value between C_{11} and C_{12},

$$C_{12} < B < C_{11}.$$

The elastic constants in Table 5.8 for tetragonal phases, $L1_0$ and DO_{22} strucutres, satisfy all of the above conditions. In particular, C_{12} is smaller than C_{11} and C_{13} is smaller than the average of C_{11} and C_{33}. The only structure that does not satisfy these stability restrictions is Mg_3Li in DO_{22} phase, thus showing mechanical instability.

Figure 5.11 presents in (a) the tetragonal shear modulus C' of our ordered bcc- and fcc-based superstructures and (b) the predicted energy difference between the corresponding bcc and fcc ordered compounds relative to hcp Mg and Li lattices, both plotted against the electron per atom ratio ranging from 1 (Li) to 2 (Mg). We find an interesting correlation between these quantities, that, in the region where bcc is very stable compared to fcc, the shear modulus is positive for bcc but negative for fcc (i.e. the fcc lattice is the mechanically unstable) and vice versa. The similar behaviour had been pointed out earlier for elemental transition metals by Craievich et al [145] and B2 and $L1_0$ TiAl by Sob et al [146]. This reflects the underlying change in hcp to fcc to bcc to hcp structural stability as the electron per atom ratio changes from 1 (Li) to 2 (Mg).

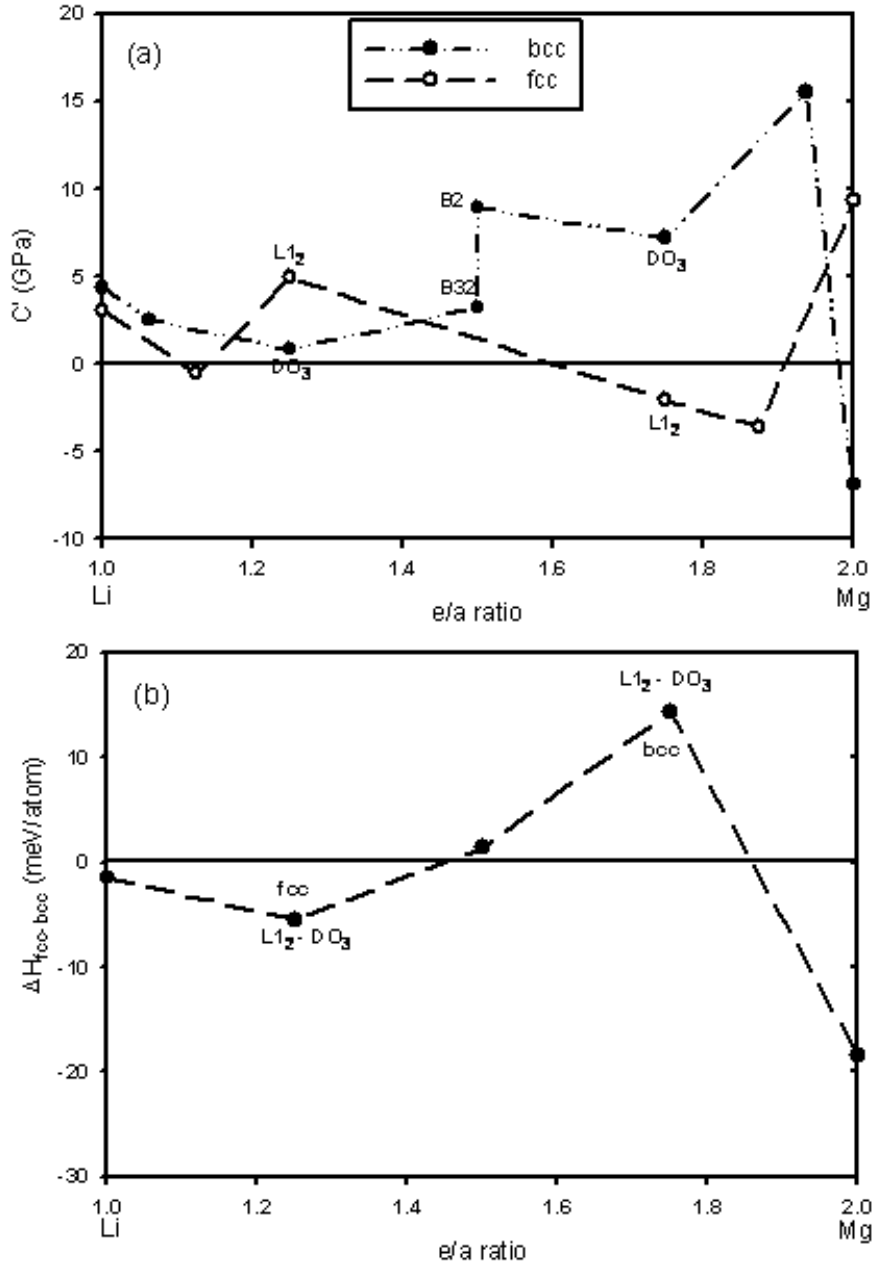

Figure 5.11: Plot of (a) tetragonal shear modulus C' of ordered bcc- and fcc-based Mg-Li superstructures and (b) the relative formation energies of the corresponding bcc and fcc Mg-Li compounds, against the electron per atom ratio.

Chapter 6
CONCLUSION AND FUTURE WORK

6.1 Conclusion

The first principles pseudopotential calculations based on the generalized gradient approximation (GGA) within density functional theory (DFT) have been utilized to succesfully investigate the cohesive, electronic and elastic properties of cubic-based Mg-Li alloys. In addition to calculating all of the equilibrium structural parameters (Sec. 5.1-5.4) we have also obtained values for all of the zero-pressure elastic constants (Sec. 5.5) for the Mg-Li compounds considered in this study.

We found that with increasing Li composition the volume shrinks and some kind of a parabolic or V-shaped trend with minimum at the equiatomic composition was observed in both fcc and bcc structures. This behaviour is clearly shown in Figure 5.1, wherein, Vegard's law [108] or Zen's law [115] , which assumes a linear dependence of the lattice constants or mean atomic volumes, respectively, of solid solutions with composition (as shown in Fig. 5.1 by solid lines), is directly violated in both fcc- and bcc-based superstructures as expected and this was also observed in earlier experiments [106] as well as previous theoretical investigations [31]. The trend of decrease in the Mg-rich region until 50 atomic per cent solute, at which the

behaviour is slowly reversed in the Li-rich region, of the lattice constant with the addition of Li for bcc structures was also obtained from earlier experiments [106].

Our results predict hcp Mg structure to be energetically favoured over the fcc and bcc structures, consistent with experimental and other theoretical results [118, 119, 120]. Our results showed that hcp Li is more stable than both fcc and bcc at zero temperature, agreeing with the experiment [7], but with only a very small energy difference (especially between fcc and hcp). Since it is known that these phases (Li) are close in energy [5, 122, 121, 123, 124, 125, 126], geometry optimizations had to be performed with great caution. As a function of concentration, the heats of formation plot shows a V-shape curve, with a minimum at the equi-concentration MgLi compound, which is in agreement with the experimental work [128] and previous theoretical results [141]. The predicted heats of formation for all the different ground state superstructures result in a representative stability profile, which shows that the DO_3, B2 and DO_{22} structures are the most stable amongst various phases having Mg_3Li, MgLi and $MgLi_3$ compositions, respectively. In both regions (Mg-rich and Li rich sides), our predicted stability profile is in full agreement with Hafner's earlier work [31] on disordered Li-Mg solid solutions.

The general trend in the total DOS is that from the bottom of the valence band the DOS increases smoothly as a function of energy as they would in a free-electron system up to E_F or just slightly above it. The Jones-analysis method compliments the

heats of formation, DOS and elastic constants results in that the predicted structural stability profile is hcp-fcc-bcc-fcc, in agreement with previous results of Hafner [31].

The bulk moduli decrease monotonically with the addition of Li content. The equation of state bulk moduli is in good agreement with both the experimental [116] and other previous theoretical [110] results. The B/C' values of 1.11, 1.18 and 1.51 for MgLi ($L1_0$), $MgLi_3$ (DO_{22}) and Mg_3Li (DO_{22}) respectively, suggest that these compounds to be brittle, while the remaining ones appear to be ductile since their values are above the critical value of 1.75. These following structures, Mg bcc, Mg_7Li, Mg_3Li ($L1_2$), Mg_3Li (DO_{22}) and $MgLi_7$ were found to be mechanically unstable. We also observed that an increase in Li content increases the Poisson ratio as well as the anisotropy.

6.2 Future work and recommendations

The predicted heats of formation with respect to different underlying lattices such as fcc or bcc will be used as an essential input for calculating effective cluster interactions, from which theoretical phase diagrams can be computed using Monte Carlo [19] or the Cluster Variation Method (CVM) [20].

The elastic moduli calculated here, in particular, Young's modulus and Poisson ratio, will serve as an input to an object oriented finite (OOF) [147] element program. This program (OOF) will be used on the micrographs (pixels) of Mg-Li samples obtained from the electron microscope (EM) to initiate microstructural studies of these

alloys. These includes simulations of stress distributions and predictions of mechanical behaviour (evolution with temperature, pressure and composition) of alloys and fracture processes.

This work will form the basis for future study in collaboration with the CSIR on the strengthening of Mg-Li alloys by the addition of ternary elements.

REFERENCES

[1] J.H. Jackson, P.D. Frost, A.C. Loonam, L.W. Eastwood, and C.H. Lorig, Trans. AIME, **185**, 149 (1948).

[2] S.S. Rajput, R. Prasad and R.M. Singru, J. Phys. Condens. Mat., **5**, 6419 (1993).

[3] B.L. Mordike and T. Ebert, Mat. Sci. and Eng. A, **302**, 37 (2001).

[4] A.A. Nayeb-Hashemi , J.B. Clark and A.D. Pelton, Bull. Alloy Phase Diagrams, **5,** 365 (1984).

[5] P. Staikov, A. Kara and T.S. Rahman, J. Phys.: Condens. Matter, **9**, 2135 (1997).

[6] C.S. Barrett, Phys. Rev., **72**, no. 3, 245 (1947).

[7] C.S. Barrett, Acta Cryst., **9**, 671 (1956).

[8] C.M. McCarthy, C.W. Thompson and S.A. Werner, Phys. Rev. B, **22**, 574 (1980).

[9] A.W. Overhauser, Phys. Rev. Lett., **53**, 64 (1984).

[10] H.G. Smith, Phys. Rev. Lett., **58**, 1228 (1987).

[11] W. Schwarz and O. Blaschko, Phys. Rev. Lett., **65**, 3144 (1990).

[12] Polmer I.J. (1989), Light alloys-Metallurgy of the light metals (New York: Chapmann and Hall, Inc).

[13] S. Schumann and H. Friedrich, The Use of Mg in Cars-Today and in Future, Conference paper at Mg Alloys and their applications, 23-30/04/98, Wolfburg, Germany.

[14] C.R. Chakravorty, Bull. Mater. Sci., Vol. 17, No. 6, November 1994, pp 733-745.

[15] Frost P.D. (1965), NASA-SP-5028 (Washington DC: NASA).

[16] A. Cottrell, Mater. Sci. Tech., **5**, 1165 (1989).

[17] A. Kelly, W.R. Tyson and A.H. Cottrell, Phil. Mag., **15**, 567 (1967).

[18] J.M. Sanchez, F. Ducastelle and D. Gratias, Physica **128A**, 334 (1984).

[19] K. Binder, in Monte Carlo Methods in Statistical Physics, Vol. 7 of Topics in Current Physics, edited by K. Binder (Springler, Berlin, 1986), p. 1.

[20] R. Kikuchi, Phys. Rev. **81**, 988 (1951).

[21] G.P. Das, A. Arya and S. Banerjee, Intermetallics, **4**, 625 (1996) and references therein.

[22] S.H. Wei, L.G. Ferreira, and A. Zunger, Phys. Rev. B, **45**, 2533 (1992).

[23] Z. Shi, M. Lin, D. Naik and J.L. Gole, J. Power Sources, **92**, 70 (2001).

[24] H. Haferkamp, W. bach and P. Juchmann, New Magnesium-Lithium alloys of higher ductility.

[25] M.C. Payne, M.P. Teter, D.C. Allan, T.A. Ariar and J.D. Joannopoulos, Rev. Mod. Phys., **64**, 1045 (1992).

[26] V. Milman, B. Winkler, J.A. White, C.J. Pickard, M.C. Payne, E.V. Akhmatskaya and R.H. Nobes, Int. J. Quantum Chem. **77**, 895 (2000).

[27] P.C. Hohenberg and W. Kohn, Phys. Rev. B, **136**, 864 (1964).

[28] A. Jayaraman, Rev. Mod. Phys., **55**, 65 (1983).

[29] E. Wimmer, Computational Methods for Atomistic Simulations of Materials,

http://www.accelrys.com/technology/qm/erich/choices/html.

[30] J.A. Majewski and P. Vogl, Chapter IV in The Structure of Binary Compounds edited by F.R. de Boer and D.G. Pettifor, Elsevier Science Publishers B.V., 1989.

[31] J. Hafner, J. Phys. F, **6**, 1243 (1976).

[32] J.C. Phillips, Phys. Rev., **112**, 685 (1958).

[33] M.L. Cohen and V. Heine, Solid State Physics, **24**, 37 (1970).

[34] J.C. Slater, Phys. Rev., **51**, 846 (1937).

[35] J.C. Slater, Quantum Theory of Molecules and Solids, Volume **4**, The self-consistent field for molecules and solids, McGraw-Hill, New York (1974).

[36] J. Korringa, Physica, **13**, 392 (1947).

[37] W. Kohn and N. Rostoker, Phys. Rev., **94**, 1111 (1954).

[38] D.D. Koelling and G.O. Arbman, J. Phys. F, **5**, 2041 (1975).

[39] O.K. Andersen, Phys. Rev. B, **12**, 3060 (1975).

[40] E. Wimmer, H. Krakauer and A.J. Freeman, Electronics and Electron Physics, ed. by P.W. Hawkes, Vol. **65**, p. 357, Academic Press, Orlando (1985) and references therein.

[41] G.B. Bachelet, D.R. Hamann and M. Schluter, Phys. Rev. B, **26**, 4199 (1982).

[42] R. Car and M. Parrinello, Phys. Rev. Lett., **55**, 2471 (1985).

[43] J.P. Perdew and Wang Yue, Phys. Rev. B, **33**, 8800 (1986).

[44] J. Labanowski and J. Andzelm, editors, Density Functional Methods in Chemistry, Springler-Verlag, New York, (1991).

[45] J.C. Slater and G.F. Koster, Phys. Rev., **94**, 1498 (1954).

[46] I. Lefebvre, M.Lannoo, and G. Allan, Phys. Rev. B, **39**, 13518 (1989).

[47] C. Mottet, G. Tréglia, and B. Legrand, Phys. Rev. B, **46**, 16018 (1992).

[48] E. Salomons, P. Bellon, F. Soisson, and G. Martin, Phys. Rev. B, **45**, 4582 (1992).

[49] R. Haydock, V. Heine, and P. J. Kelly, J. Phys. C, **5**, 2845 (1972), **8**, 2591 (1975).

[50] P. Turchi and F. Ducastelle, The Recursion Method and Its Applications, D. G. Pettifor and D. L. Weaire, editors, Springer-Verlag, Berlin p. 104 (1985).

[51] M. Aoki, Phys. Rev. Lett., **71**, 3842 (1993).

[52] D.G. Pettifor, Phys. Rev. Lett., **63**, 2480 (1989).

[53] D.R. Bowler, M. Aoki, C.M. Goringe, A.P. Horsfield and D.G. Pettifor, Modelling Simul. Mater. Sci. Eng., **5**, 199 (1997).

[54] S. Znam, D. Nguyen-Manh, D.G. Pettifor and V. Vitek, Phil. Mag., **83**, 415 (2003).

[55] D.R. Hartree, Proc. Camb. Phil. Soc., **24**, 89 (1928).

[56] V. Fock, Z. Phys., **61**, 126 (1930) and ibid **62**, 795 (1930).

[57] C. Møller and M.S. Plesset, Phys. Rev., **46**, 618 (1934).

[58] A.V. Krasheninnikov, Lectures on Introduction to electronic structure calculations,

www.acclab.helsinki.fi/~akrashen/esctmp.html.

[59] L.H. Thomas, Proc. Camb. Phil. Soc., **23**, 542 (1927).

[60] E. Fermi, Z. Physik, **48**, 73 (1928).

[61] J. Kohanoff and N.I. Gidopoulos, Density Functional Theory: Basics, New Trends and Applications Vol. 2, Part 5, Chapter 26, pp 532, in Hanbbook of Molecular Physics and Quantum Chemistry, John Wiley & Sons, Ltd, Chichester, 2003.

[62] M. Born and R. Oppenheimer, Ann. Physik, **84**, 457 (1927).

[63] W. Kohn and L.J. Sham, Phys. Rev. A, **140**, 1133 (1965).

[64] F. Bloch, Z. Physik, **57**, 545 (1929).

[65] J. Hafner, Acta Mater, **48,** 71-92 (2000).

[66] J.P. Perdew, J.A. Chevary, S.H. Vosko, K.A. Jackson, D.J. Singh and C. Fiolhais, Phys. Rev. B, **46**, 6671 (1992).

[67] E. Hult, Y. Andersson and B.I. Lundqvist, Phys. Rev. Lett., **77**, 2029 (1996).

[68] W. Kohn, Y. Meir and D.E. Makarov, Phys. Rev. Lett., **80**, 4153 (1998).

[69] J.P. Perdew, Phys. Rev. B, **33**, 8822 (1986).

[70] A.D. Becke, Phys. Rev. A, **38**, 3098 (1988).

[71] J.P. Perdew and Y. Wang, Phys. Rev. B, **45**, 13244 (1992).

[72] J.P. Perdew, K. Burke and M. Ernzerhof, Phys. Rev. Lett., **77**, 3865 (1996).

[73] G. Kresse, J. Furthmüller and J. Hafner, Phys. Rev. B, **50**, 13181 (1994).

[74] T.C. Leung, T.C. Chan and B.N. Harmon, Phys. Rev. B, **44**, 2923 (1991).

[75] T. Asada and K. Terakura, Phys. Rev. B**, 47**, 15992 (1993).

[76] J.P. Perdew and A. Zunger, Phys. Rev. B, **23**, 5048 (1981).

[77] D.M. Ceperly and B.J. Alder, Phys. Rev. Lett., **45**, 566 (1980).

[78] J.P. Perdew, K. Burke and M. Ernzerhof, Phys. Rev. Lett. **78**, 1396 (E) (1997).

[79] E.H. Lieb and S. Oxford, Int. J. Quantum Chem., **19**, 427 (1981).

[80] P. Ravindran, L. Fast, P.A. Korzhavyi, B. Johansson, J. Willis and O. Eriksson, J. App. Phys. **84**, 4891 (1998).

[81] M.J. Mehl, B.M. Klein, and D.A. Papaconstantopoulos, Intermetallic Compounds: Vol. 1, Principles. Edited by J.H. Westbrook and R.L. Fleischer, 1994, John Wiley & Sons Ltd.

[82] N.W. Ashcroft and N.D. Mermin, Solid State Physics, Saunders College, Philadelphia (1976).

[83] M.J. Mehl, Phys. Rev. B, **61**, 1654 (2000).

[84] J.F. Nye, Physical Properties of Crystals, Clarendon, Oxford (1957).

[85] D.C. Wallace, Thermodynamics of Crystals (Wiley, New York, 1972), Chapter 1.

[86] D. Iotova, N. Kioussis and S.P. Lim, Phys. Rev. B, **54**, 14413 (1996).

[87] S.F. Pugh, Philos. Mag. **45**, 823 (1954).

[88] W. Koster and H. Franz, Metall. Rev., **6**, 1 (1961).

[89] M.H. Ledbetter, Materials at Low Temperatures, edited by R.P. Reed and A.F. Clark, p. 1.

[90] W.A. Harrison, Electronic Structure and the Properties of Solids, edited by Freeman, San Francisco (1980).

[91] M.J. Gillan, Computer Simulation in Materials Science , edited by M. Meyer and V. Poutikis (Dordrecht: Kluwer) p. 257 (1991).

[92] N. Troullier and J.L. Martins, Phys. Rev. B, **43**, 1993 (1991).

[93] J.S. Lin, A. Qteish, M.C. Payne and V. Heine, Phys. Rev. B, **47**, 4174 (1993).

[94] A.M. Rappe and J.D. Joannopoulos, Computer Simulation in Materials Science ed M. Meyer and V. Poutikis (Dordrecht: Kluwer) p. 409 (1991).

[95] D. Vanderbilt, Phys. Rev. B, **41**, 7892 (1990).

[96] M.D. Segall, P.L.D. Lindan, M.J. Probert, C.J. Pickard, P.J. Hasnip, S.J. Clark and M.C. Payne, J. Phys. Cond. Matt., **14**, 2717 (2002).

[97] F. Wagner, Th. Laloyaux and M. Scheffler, Phys. Rev. B, **57**, 2102 (1998).

[98] M.J. Gillan, J. Phys.: Condens. Matter **1**, 689 (1989).

[99] Grotheer and Fähnle, Phys. Rev. B, **58**, 13459 (1998).

[100] Y. Mishin, D. Farkas, M.J. Mehl and D.A. Papaconstantopoulos, Phys. Rev. B, **59**, 3393 (1999).

[101] O. Le Bacq, F. Willaime and A. Pasturel, Phys. Rev. B, **59**, 8508 (1999).

[102] H. Hellmann, Einfukrung in die Quantumchemie (Deuticke, Leipzzig,1937), pp. 61 and 285; R.P. Feynman, Phys. Rev., **56**, 340 (1939).

[103] P. Pulay, Molec. Phys., **17**, 197 (1969).

[104] H.J. Monkhorst and J.D. Pack, Phys. Rev. B, **13**, 5188 (1976).

[105] W. Pitsch, in Phase Stability in High Temperature Alloys, edited by V. Guttmann (Applied Science Publishers, London, 1981), p. 1.

[106] D.W. Levinson, Acta Met., **3**, 294 (1955).

[107] F.H. Herbstein and B.L. Averbach, Acta Met., **4**, 407 (1956).

[108] L. Vegard, Z. Phys., **5**, 17 (1921).

[109] V.G. Vaks and A.V. Trefilov, J. Phys. F: Met. Phys., **18**, 213 (1998).

[110] H.L. Skriver, Materials Science Databases, CAMP, DTU, http://databases.fysik.dtu.dk/.

[111] B.R. Sahu, Mat. Sci. Eng. B, **49**, 74 (1997).

[112] J. Hafner and W. Weber, Phys. Rev. B, **33**, 747 (1986).

[113] S.H. Kellington, D. Loveridge and J.M. Titman, Brit. J. Appl. Phys. (J. Phys. D), Ser. 2, Vol. 2, 1162 (1969).

[114] R. Laihia, K. Kokko, K. Mansikka and P.T. Salo, J. Phys. C, **6**, 10247 (1994).

[115] E-an Zen, Am. Mineral, **4**, 523 (1956).

[116] R.W. Lynch and L.R. Edwards, J. Appl. Phys., **41**, 5135 (1970).

[117] A. Cottrell, An Introduction to Metallurgy, Second Edition ,1975.

[118] L. Kaufman and H. Bernstein, Computer Calculation of Phase Diagrams (Academic, New York, 1970).

[119] A.K. McMahan and J.A. Moriarty, Phys. Rev. B, **27**, 3235 (1983).

[120] H.J. Gotsis, D.A. Papaconstantopoulos and M.J. Mehl, Phys. Rev. B, **65**, 134101 (2002).

[121] K. Doll, N.M. Harrison and V.R. Saunders, J. Phys.: Condens. Matter, **11**, 5007 (1999).

[122] M.M. Dacorogna and M.L. Cohen, Phys. Rev. B, **34**, 4996 (1986).

[123] J.A. Nobel, S.B. Trickey, P. Blaha and K. Schwarz, Phys. Rev. B, **45**, 5012 (1992).

[124] J.C. Boettger and R.C. Albers, Phys. Rev. B, **39**, 3010 (1989).

[125] A.Y. Liu, A.A. Quong, J.K. Freericks, E.J. Nicol and E.C. Jones, Phys. Rev. B, **59**, 4028 (1999).

[126] H. Bross and R. Stryczek, Phys. Status Solidi B, **144**, 675 (1987).

[127] N. Saunders, A.P. Miodownik and A.T. Dinsdale, CALPHAD, **21**, 351 (1988).

[128] V.P. Mashovetz and L.V. Puchkov, Zh. Prikl. Chem., 1875 (1965).

[129] F. Ducastelle, Order and phase stability in alloys Vol. 3, 1991, Elsevier (Netherlands).

[130] C. Kittel, Introduction to Solid State Physics, 7th Edition, 1996, John Wiley & Sons, Inc., New York.

[131] D.G. Pettifor, Bonding and Structure of Molecules and Solids, Oxford University Press Inc., New York (1996).

[132] J. -H. Xu, T. Oguchi and A.J. Freeman, Phys. Rev. B, **35**, 6940 (1987).

[133] I.A. Abrikosov, Yu.H. Vekilov, P.A. Korzhavyi, A.V. Ruban and L.E. Shilkrot, Solid State Comm. **83**, 867 (1992).

[134] H. Jones, Proc. Phys. Soc. A, **49**, 250 (1937).

[135] O.K. Andersen, O. Jepsen and M. Sob, Electron Band Structure and its Applications, edited by M. Yossouff, Springer-Verlag, Berlin, 1987.

[136] H.L. Skriver, The LMTO method (Springer-Verlag, Berlin, 1984).

[137] J. Chen, L.L. Boyer, H. Krakauer, and M.J. Mehl, Phys. Rev. B, 37, 3295 (1988).

[138] M.J. Mehl and L.L. Boyer, Phys. Rev. B, 43, 9498 (1991).

[139] O.H. Nielsen and R.M. Martin, Phys. Rev. B, **32**, 3780 (1985), **32**, 3792 (1985).

[140] L. Kleinman, Phys. Rev., 128, 2614 (1962).

[141] P. Beauchamp, R. Taylor and V. Vitek, J. Phys. F. Metal Phys. **5**, 2017 (1975).

[142] A. Zhu, B.M. Gable, G.T. Shiflet and E.A. Starke Jr., Acta Mater. **52**, 3671 (2004).

[143] R. A. Felice, J. Trivisonno, D. E. Schuele, Phys. Rev. B, **16**, 5173 (1977).

[144] G. Simmons and H. Wang, Single Crystal Elastic Constants and Calculated Aggregate Properties: A handbook, 2nd ed. (MIT Press, Cambridge, Massachusetts, 1971).

[145] P.J. Craievich, M. Weinert, J.M. Sanchez and R.E. Watson, Phys. Rev. Lett., **72**, 3076 (1994).

[146] M. Sob, L.G. Wang and V. Vitek, Comp. Mat. Sci., **8**, 100 (1997).

[147] S.A. Langer, W.C. Carter and E.R. Fuller Jr.,OOF, NIST, Gaithersburg, MD,1997.

[148] X.Q. Guo, R. Podloucky and A.J. Freeman, Phys. Rev. B, **42**, 10912 (1990).

Appendix A
Papers presented at Local and International Conferences

Oral Presentations

1. Cohesive, electronic and elastic properties of cubic-based Mg-Li alloys, 7th Annual Materials Modelling Meeting (MMM), 2004, University of the North, Sovenga, SA.
2. Cohesive and elastic properties of ordered cubic-based Mg-Li alloys, 48th South African Institute of Physics (SAIP) Annual Conference, 2003, University of Stellenbosch, Stellenbosch, SA.
3. A computational study of structural, electronic and elastic properties of cubic-based Mg-Li alloys, 5th and 6th Annual MMM 2002-3, University of the North, Sovenga, SA.
4. Ab initio study structural, electronic and elastic properties ordered cubic-based Mg-Li alloys, 47th SAIP Annual Conference, 2002, Potchefstroom University, Potchefstroom, SA.
5. Ab initio study of structural, electronic and elastic properties of cubic-based Mg-Li alloys, Unin Post-graduate Society, 2002, University of the North, Sovenga, SA.
6. Cohesive, Electronic and Elastic Properties of ordered Mg-Li alloys,

Royal Society-National Research Foundation Programme, 2004, Pretoria, SA.

Posters Presentations

1. Structural and Electronic properties of ordered Mg-Li compounds, 49th South African Institute of Physics (SAIP) Annual Conference, 2004, University of Free-State, Free-State, SA.
2. Cohesive properties of cubic-based Mg-Li alloys, CCP5 Summer School 2003, King's College, London, UK.
3. A study of structural properties of Mg-Li alloys, 46th SAIP Annual Conference, University of Natal, Durban, 2001, SA.
4. A study of structural properties of Al-Cu alloys, 4th Annual MMM 2001, University of the North, Sovenga, SA.